COMMONS DEED

저작자표시-비영리-변경금지 2.0 대한민국

이용자는 아래의 조건을 따르는 경우에 한하여 자유롭게

- 이 저작물을 복제, 배포, 전송, 전시, 공연 및 방송할 수 있습니다.

다음과 같은 조건을 따라야 합니다:

저작자표시. 귀하는 원저작자를 표시하여야 합니다.

비영리. 귀하는 이 저작물을 영리 목적으로 이용할 수 없습니다.

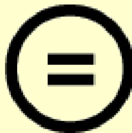

변경금지. 귀하는 이 저작물을 개작, 변형 또는 가공할 수 없습니다.

- 귀하는, 이 저작물의 재이용이나 배포의 경우, 이 저작물에 적용된 이용허락조건을 명확하게 나타내어야 합니다.
- 저작권자로부터 별도의 허가를 받으면 이러한 조건들은 적용되지 않습니다.

저작권법에 따른 이용자의 권리는 위의 내용에 의하여 영향을 받지 않습니다.

이것은 이용허락규약(Legal Code)을 이해하기 쉽게 요약한 것입니다.

Disclaimer

dCollection

이학박사 학위논문

전극-절연막-용액 시스템의 전도현상의 이해 및 나노전기변색 소자로의 응용

Conduction of Thin Dielectric Film in Contact with Solution and Its Application to Nano-Electrochromic Devices

2019년 8월

서울대학교 대학원
화학부 전기화학전공
윤 정 세

Abstract

The conduction in the dielectric materials has been regarded as an important issue for electronic devices. Recently, the operating condition of devices that employing oxides has expanded to wet condition such as in batteries, energy conversion devices, and electrochemical field effect transistors. For enhanced device performance, a deeper understanding of its conduction and breakdown mechanism should be preceded. In this dissertation, therefore, the electrical and ionic conduction of oxide dielectrics in contact to the electrolyte is understood in the electrolyte/oxide/semiconductor system. Especially, the role of chemical species which are dissolved in the electrolyte is revealed, focusing on their effect on the physical and chemical nature of the oxide-electrolyte interface. Not only the basic principles of conduction in dielectric oxides but also a new application field of cation conductive oxide is suggested in this dissertation. When dielectrics or large bandgap semiconductors allow the introduction of ionic species from electrolyte to the matrix by means of the electrical potential applied on the underlying electrode, their optical properties are changed, which is called electrochromism. There are numerous studies regarding on electrochromism, however, the scope of

application is limited because the wide color expression and the dynamic color tunability has not been achieved. To overcome these problems, the structure around the electrochromic oxide, WO_3, is thoroughly designed for tunability in the visible regime. By employing nanometer-thick WO_3 film in the structure, full-color tunable reflective- and transmissive- type devices are achieved with the advantages of reversibility and low energy consumption.

Keywords: electrode/oxide/semiconductor system, dielectric breakdown, dielectric thin film, electrochromism, WO_3, nano optics

Table of Contents

1. Introduction ……………………………………………………………10

2. Conduction of Dielectric Material in Contact to Electrolyte ……...14

2.1. Introduction: Related issue on Charge Conduction of SiO2 and Si3N4 in Contact to Electrolyte ……………………………………………….....14

2.2. Theoretical Background ……………………………………………..16

2.2.1. Conduction of thin dielectric film in solid state device ……….16

2.2.2. Dielectric breakdown ………………………………………..........22

2.2.3. Electrolyte/oxide/semiconductor (EOS) system ....…24

2.3. Experimental Section ……………………………………………28

2.3.1. Materials ………………………………………………………...28

2.3.2. Preparation of dielectric film-coated Si electrode ...………………28

2.3.3. Protective layer coatings on Si/SiO2 ……………………………28

2.3.4. Electrochemical characterization ……………………………..29

2.3.5. Theoretical calculation …………………………………………30

2.4. Results ………………………………………………………………32

2.4.1. Electrochemical analysis of large-area dielectrics. Effect of unwanted damage and misunderstandings due to the inevitable defects ……….32

2.4.2. Methods for minimizing experimental deviation ………………...36

2.4.3. General electrochemical behavior of defect-suppressed dielectrics in contact to solution ………………………………………………………39

2.4.4. Cation effect on dielectric breakdown characteristics: sodium intercalation and accelerated breakdown kinetics ………………………42

2.4.5. Electron scavenger effect on dielectric breakdown characteristics: non-destructive conducting pathway by electron scavenger…………………52

2.4.6. Postbreakdown phenomena ……………………………………58

2.5. Summary ………………………………………………………………65

3. Full-color-tunable Electrochromic Device Using Tungsten Trioxide Thin Film ……………………………………………..………………..68

3.1. Introduction: Electrochromic Device and Nanostructure for Better Optical Performance ……………………………………………..…68

3.2. Experimental Section ……………………………………..……...71

3.2.1. Reagent and Appartus …………………………………………...71

3.2.2. Deposition of WO3 films ……………………………….…....71

3.2.3. Preparing WO3 coated Si electrode for optical and electrochemical analysis ……………………………………………………………………...72

3.2.4. Electrochemical analysis…………………………………………...72

3.2.5 Optical analysis ……………………………………...………...73

3.2.6. Fabrication of reflective- and transmissive- type device …..…...73

3.3. Results and discussion …………………………………….....75

3.3.1. Analysis on tungsten trioxide thin film …………………………..75

3.3.2. Reflective type display using WO3 thin film ………………...85

3.3.3. Transmissive type display using WO3-based thin film ……....90

3.4. Summary ………………………………………………………94

4. Conclusion ………………………………………………………95

Reference ………………………………………………………97

List of Figures

Figure 1. Schematic diagrams of conduction model of (a) Fowler-Northernheim tunneling, (b) hopping conduction, (c) Poole-Frenkel emission and (d) ionic conduction which are summarized in section 2.2.1. 17

Figure 2. A schematic diagram of EOS system under cathodic bias. 24

Figure 3. Cyclic voltammograms of Si/6 nm SiO_2 electrode at electrolytes containing (a) oxidized form of redox molecules and (b) a reduced form of redox specie...33

Figure 4. Cyclic voltammograms of Si/6 nm SiO_2 electrode conducted at the electrolyte containing (a) ferricyanide and (b) ruthenium hexamine (III) at different pH. 34

Figure 5. (a) A schematic diagram and (b) a photograph of the electrochemical cell for minimizing chemical and physical damage that possibly applied to SiO_2 layer. Alumina and photoresist define the exposed area of SiO_2 to be 50×50 μm^2. Whole silicon wafer serves as a working electrode to minimize unwanted physical damage during dicing or manual handling. 36

Figure 6. Cyclic voltammograms of area confined SiO_2 (50×50 μm^2) with the thickness of (a) 6 nm and (b) 10 nm. 39

Figure 7. (a) A current-time curve of Si/6nm SiO_2 electrode under constant voltage (−4 V) stress and (b) its magnification of low current region. 41

Figure 8. Breakdown potential (V_{db}) of Si/10 nm SiO_2 electrode obtained at the

electrolytrytes varying (a) cations, (c) Na^+ concentration and (d) anions. Breakdown potential of Si_3N_4 with different cation is presented in (b) 42

Figure 9. V_{db}-pH dependence of Si/10 nm SiO_2 electrode obtained at aqueous electrolytes containing (a) 0.5 M NaCl, (b) 1 mM NaCl, and (c) 0.5 M KCl. (d) V_{bd}-pH dependence of Si/10 nm Si_3N_4 electrode at aqueous buffer containing 0.5 M NaCl. 43

Figure 10. Expected potential gradient of EOS system (left) without and (middle, right) with cation species that can transport to SiO_2 from electrolyte...........46

Figure 11. (a) Normalized free energy required to cation transport from aqueous to SiO_2 phase. (b) Mean displacement of cations versus time for different alkali metal cations calculated by molecular dynamic simulation. 48

Figure 12. (a) V_{bd} of Si/10 nm SiO_2 electrode obtained at organic solvent (acetonitrile) based electrolyte containing 0.1 M of $LiClO_4$, $NaClO_4$, $TBAClO_4$ electrolytes. The saturated $KClO_4$ electrolyte was used due to its low solubility. (b) Calculated normalized relative stability of when alkali cation is transferred from acetonitrile to SiO_2. Data obtained from SiO_2-water system is also presented for comparison. 50

Figure 13. (a) V_{bd} and (b) Weibull plot of Si-SiO_2 Si/10 nm SiO_2 electrode broken down at aqueous electrolyte with or without 10 mM ruthenium hexamine (III) in 0.5 M KCl buffered by 50 mM phosphate buffered solution (pH 3). 52

Figure 14. 3D-scatter plot of sampled current obtained at -7 V during negative potential sweep of Si/10 nm Si_3N_4 electrode varying temperature (x-axis)

and pH (y-axis)..55

Figure 15. (a) Mean flowed charge until breakdown during the potential sweep at each condition. (b) Mean breakdown potential measured at each condition.56

Figure 16. SECM images for a 200×200 μm^2 Si/6 nm SiO_2 substrate electrode obtained in a SG-TC mode, monitoring the $[Ru(NH_3)_6]^{2+}$ oxidation current of a tip with a tip potential (E_{tip}) held at −0.5 V in 10 mM $[Ru(NH_3)_6]Cl_3$/0.1 M PBS (pH 3) applying −1 V to the Si/SiO_2 substrate. Distance of tip to substrate is 10 μm. Scan rate is 50 μm s^{-1}. The unit of tip current is nA. (a) Before breakdown and (b) right after breakdown at −4 V in 0.1 M PBS (pH 3). After additional (c) 750-s and (d) 800-s voltage of −4 V application to the Si/SiO_2 substrate of (b) in 0.1 M PBS. (e) A SECM image for 200×200 μm^2 Si/SiO_2 substrate electrode obtained in a normal feedback mode, monitoring the $[Ru(NH_3)_6]^{3+}$ reduction current of a tip with a tip potential (E_{tip}) held at −0.5 V (vs. SCE) in 10 mM $[Ru(NH_3)_6]Cl_3$ dissolved in 0.1 M PBS (pH 3) without applying any potential to the Si/SiO_2 substrate. Distance of tip to substrate = 10 μm. Scan rate = 50 μm s−1. The tip current scale is nA.......58

Figure 17. Representative SEM and TEM images of the inverted pyramid structure resulted from cathodic breakdown and post breakdown etching. SEM images of (a) top-view and (b) cross sectional side view of the yellow dotted line in (a). Cross sectional TEM image of (c) undamaged Si(100) surface (yellow-dotted circle in (b)) and (d) sidewall of the inverted pyramid structure which has Si(111) surface with many steps (red-dotted circle in (b)).....................61

Figure 18. A schematic of Si/SiO_2 breakdown mechanism in acidic condition. 63

Figure 19. Cyclic voltammograms of WO_3 film deposited on highly doped Si substrate in 100 mM $LiClO_4$ electrolyte (acetonitrile) varying (a) thickness and (b) scan rate. 76

Figure 20. Steady state potential and diffusion coefficient of Li in Li_xWO_3 obtained via galvanostatic intermittent titration technique (GITT). 78

Figure 21. X-ray photoelectron spectra of (left) as-prepared WO_3 film in the region of W (upper-left) and O (bottom-left). X-ray photoelectron spectra of WO_3 after Li intercalation are presented on the right column in the region of W (upper-right) and O (bottom-right)...80

Figure 22. X-ray diffraction spectrum of WO_3 thin film deposited on highly doped Si wafer. 81

Figure 23. Scanning electron microscopy image of (a) as-sputtered WO_3 film and (b) WO_3 after Li intercalation/de-intercalation cycle...................................82

Figure 24. Optical properties of WO_3 thin film as a function of the amount of Li^+ injection. (a) Refractive index and (b) absorption coefficient measured with a range of wavelength between 350 nm to 1650 nm.......................................83

Figure 25. Schematic illustration of color generation and tuning mechanism of reflection-type device..85

Figure 26. (a) Reflectance of WO_3 thin film on Si as a function of the incident wavelength and the thickness of WO_3. (b) Photographic image of fabricated

red, green, and blue samples with target thickness. (c) Calculated (top) and experimental (bottom) spectra of reflected light. Color variation corresponding to each same colored spectrum from state 1 through 4 to 6 (inset). 86

Figure 27. The reversibility and stability test of the reflective type devices. The spectrum change of a 235 nanometer-thick WO_3 on Si at state (a) 1 and (b) 6 for different Li^+ intercalation cycles. (c) The reflected spectra of a 165 nanometer-thick WO_3 on Si of state 6 after immersed in electrolyte............88

Figure 28. Schematic diagrams representing the working principle of transmissive type electrochromic device. 90

Figure 29. (a) Simulated transmittance of Ag/WO_3/Ag on quartz substrate as a function of the incident wavelength and the thickness of WO_3. (b) Photograph of primary devices (R, G and B) operates in transmissive type. (c) Simulated spectra tuning of transmitted light for R, G and B (top). Experimental spectra of transmissive devices showing switching capability. 92

1. Introduction

Metal and semiconductor oxides have been imperative material for modern technology. They not only serve as important components in electronic device,[1] optical materials,[2,3] and passivation layers[4–8] but also are considered to be prominent materials for future technology such as resistive random access memory devices,[9,10] batteris[11–14] and transistors gated by electrochemical principles[15]. These technologies require the deeper understandings of the chemical nature of the oxides, because their key phenomena are complex chemical reactions in the oxide such as the formation of defects in the oxide lattice and the mass transport of O^{2-}, [16,17] H^{+}, [18–22] alkali cations[23–25] etc. In general, the devices using the oxide normally operate in contact to other solid or gas phase, however, batteries and electrochemical transistors operate in the electrochemical environment where they are working in contact to electrolyte. The difference in working condition offers significant chances to interact with chemical species present in the liquid phase, electrolyte. These species are possibly get involved in the device operation by changing the character of oxide-electrolyte interface or by exchanging charge through electrochemical reactions.

There have been numerous reports to address electronic and ionic conduction in the insulating oxide films.[26–28] For the ionic conduction, the transportation of oxygen anion has received a lot of attentions because of the switching conductivity of the film arises from the partial reduction of oxides accompanied with O^{2-} diffusion.[16,17] Cations which reside and diffuse inside the oxide have been regarded

as a main reason of device failure.[18,24,29] The origin of cationic species are considered to be alkali metal impurity implanted during the fabrication process, or the cations intercalated from outside by the potential gradient or thermal energy applied to the oxide.[30]

Among the cations, the existence of mobile protons in the insulating oxide has been reported with experimental[31–34] and computational evidences.[19,20] One important issue on the cationic transport is a role of protons in ionic conduction. The ambiguity of the role of protons is resulted from the complexity of the amorphous insulating film, which varies greatly in physical and chemical properties depending on each manufacturing method. For example, some literatures regard the proton diffusion as natural in SiO_2,[31,32,35] otherwise others rarely consider proton due to its small diffusivity compared to the diffusion of other alkali metal cations.[30]

Another aspect that is missing during discussing the cation transport property of various insulating film is their interface. The interface of oxides is comprised of inhomogeneous chemical structure different from that of bulk phase, thus they show unique characteristics of surface. One of them is surface potential built on the interface.[36] The surface potential at electrolyte-oxide interface is built by the dipole induced by the protonation of surface functional group, and this dipole could highly affect not only the interfacial mass transport of charged species but also the overall electric field applied across the oxide film.

Not only the ionic conduction, but also the electronic conduction of oxide

immersed in electrolyte requires further understanding. When the charge carriers injected to the oxide are flow to the adjacent solid phase such as metal and semiconductor, the resistance of interfacial charge transfer would be negligible because of the large density of states in metals and semiconductor. On the other hand, the rate of charge transfer would be rather slower at the oxide/electrolyte interface because the hot carriers in the oxide should be ejected through electrochemical reaction of molecules in the electrolyte or adsorbates in the oxide/electrolyte interface. Thus the overall conductivity would be modulated by modifying the electrochemical environment of electrolyte, however there is little number of researches regarding on this phenomena.

Therefore, in this dissertation, the conduction of electrolyte/oxide/semiconductor (EOS) system under electric field will be discussed. In chapter 2, the factors which can possibly affect the electrical behavior of EOS system are analyzed experimentally, including dielectric breakdown kinetics. The existing theories and related issues when oxide film is contained in solution are summarized. The electrode of insulating film on highly doped Si was used, incorporating widly used dielectric materials, SiO_2 and Si_3N_4 which are known to be good dielectric materials. An experimental methodology for obtaining reliable data will be proposed. The effect of the chemical environment of the solution on EOS system is experimentally confirmed and theoretically explained. The pH, the ion environment and the electrochemical reactant of the electrolyte were varied and the roles of them are evaluated both in quantitative and qualitative manners. To achieve this goal, breakdown potential (V_{db}), charge flowed until

breakdown (Q_{db}) and time for breakdown (t_{db}) under voltage bias are precisely measured and analyzed. The experimental results and the explanation on them are supported with the aid of computational methods, density functional theory and molecular dynamic calculations.

In chapter 3, an oxide material which allows both ionic conduction and electric conduction are employed. The well-known cation conductor, WO_3, has drawn a lot of interest due to its promising applicability such as electrochromic devices,[3] photocatalysts,[37] electrochemical gating devices[15] and batteries. Most works used thick WO_3 film to achieve electrochromic devices which show enough light tunability when cations are intercalated. For the thickness of the film, they could switch the transparency with two modes, pale and dark modes. However, they cannot express various colors, losing the color dynamicity. In this thesis a nanometer-thick WO_3 film is placed in the uniquely designed structures not only to express wide color in visible but also to tune and switch their optical property. A reflective- and a transmissive-type devices are suggested and their light tunability is evaluated quantitatively. Before the device fabrication, fundamental understandings are preceded for the reasonable design of devices.

2. Conduction of Dielectric Material in Contact to Electrolyte

2.1. Introduction: Related issue on Charge Conduction of SiO_2 and Si_3N_4 in Contact to Electrolyte

SiO_2 and Si_3N_4 are a widely used material due to its earth abundance and its electrical property. The conductivity of SiO_2 and Si_3N_4 has been studied mainly in terms of the stability and reliability of electronic devices.[38,39] Therefore, most of the studies have been conducted for solid-state devices. However, the deeper understanding of conduction on these systems is required because many systems incorporating dielectric materials that have been studied these days operate in contact with vapor and liquid phase. Especially for ionic conduction inside SiO_2, the experimental model systems of previous reports have been made forcibly by ion implantation, i.e. Na^+ or K^+, during the fabrication process.[24,25,40,41] Therefore, such ion conduction in the model systems would not represent the ion conduction in intrinsic SiO_2.

As far as I know, the understandings on conductivity of dielectric oxide when it has an interface with solution are as follows. It is known that current hardly flows at as-prepared-dry SiO_2[42], but it becomes conductive after being exposed to acidic solution for a long time, or its conductivity depends on the quality of the film.[32,43–

[45] Other insulating films such as Si_3N_4, HfO_2[35,46] and Al_2O_3[11,12,47,48] in contact with the solution have been studied, and these studies have some insights into the conduction of SiO_2. They have reported the correlation between the solution environment and the conduction of the insulating film, but the exact mechanism has not been analyzed in detail.

From this point of view, the following issues need to be addressed. Can the ions in the solution enter the oxide membrane and be conducted? What is the exact role of proton in the conduction of the oxide film? How important is the charge transfer rate at the interface for the conduction of the EOS system? In order to answer these questions, in this dissertation, the dielectric breakdown of SiO_2 is investigated in the system composed of highly doped Si-SiO_2-electrolyte with negative potential applied to the Si side. Dielectric breakdown is a phenomenon that an insulator loses insulation when an electric field is applied. The chemical structure of the insulator is irreversibly destroyed after the dielectric breakdown.[38] The kinetics of dielectric breakdown is closely related to the electric charge flowed through the insulator. Therefore, by studying dielectric breakdown, it is possible to figure out electron and ion conduction, and electric field distribution in an insulating film.

2.2. Theoretical Background

2.2.1. Conduction of thin dielectric film in solid state device

There are multiple mechanisms which describe electrical conduction of dielectric films. The mechanisms can be categorized into two types; electrode-limited and bulk-limited conduction. The electrode-limited conduction postulates ideal dielectric materials, whose chemical structure is homogeneous thus has no defect in the material. Because the charge carrier injection is carried out by overcoming the energy barrier between dielectrics and adjacent electrode, the conduction is dominated by the electrode-dielectric junction. Current is delivered by the charge carriers in the dielectrics which are electrons for the conduction band and holes for the valence band, and these carriers are injected from the metals or semiconductors nearby. Current can also be flowed by the direct tunneling through the dielectric film. Bulk-limited conduction is happened when there are defects in chemical structure, which can trap the charge carriers, electrons, holes and ions. Rather than charge is directly injected to the conduction and valence band, the current flow is mediated by defect states which are located in between conduction and valence band of dielectrics.

These mechanisms are well evidenced by numerous studies. Equations which describe each mechanism are constructed and the equations are successfully fit the

experimental results. Among the reported mechanisms, four mechanisms listed below are expected to happen in the n^+-Si/SiO_2(or Si_3N_4)/electrolyte system which is model system in this thesis. Here the brief summary of each conducting mechanism is presented based on the review reported by Chiu et al.[26]

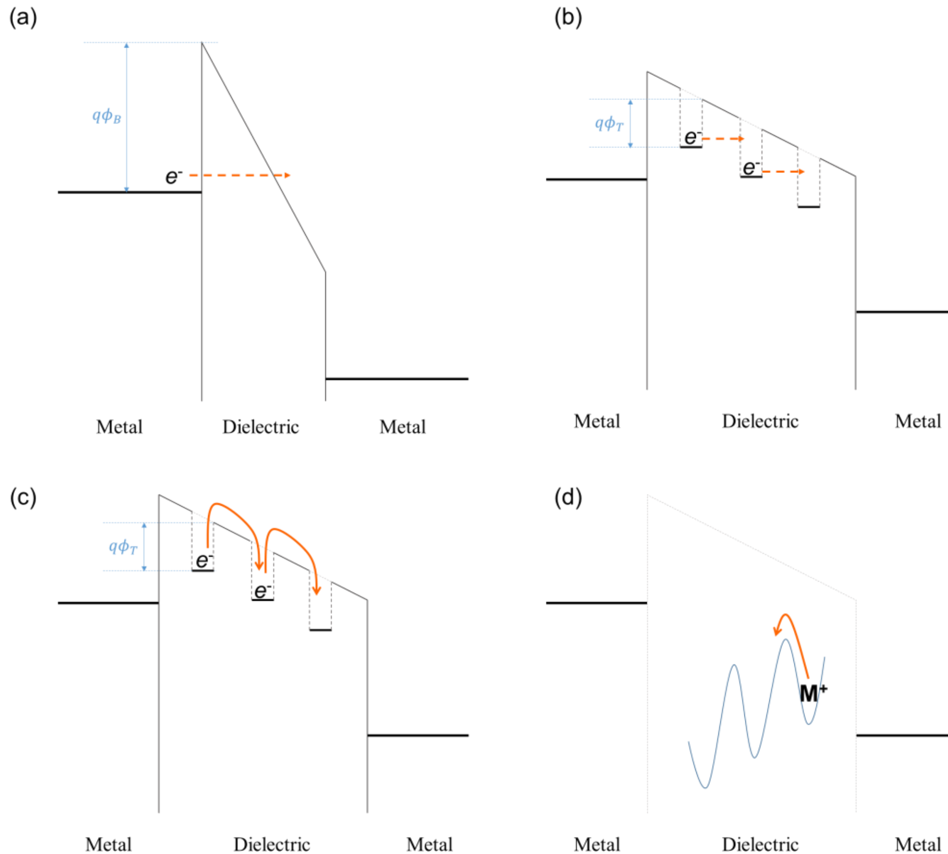

Figure 1. Schematic diagrams of conduction model of (a) Fowler-Northernheim tunneling, (b) hopping conduction, (c) Poole-Frenkel emission and (d) ionic conduction which are summarized in section 2.2.1.

Fowler-Northernheim (FN) tunneling

Among the electrode-limited conduction mechanisms, FN tunneling addresses the conduction of thick oxide where direct tunneling hardly happens. Thus FN tunneling requires large potential difference in general. The electrons in the electrode tunnel through the triangular quantum barrier, and they are injected to the conduction band (Figure 1a). The equation which describes this mechanism is

$$J = \frac{q^3 E^2}{8\pi h q \phi_B} \exp\left[\frac{-8\pi (2 q m_T^*)^{1/2}}{3hE} \phi_B^{3/2}\right] \text{……………………..(eq.1)}$$

where J is the current density, E is the electric field applied to the dielectric, h is he Plank's constant, $q\phi_B$ is the Schottky barrier height, m_T^* is the effective tunneling mass in dielectric , q is the electronic charge.

The major characteristic of this conduction mechanism is its temperature independency and linear relationship between $\ln(J/E^2)$ and $1/E$. This plot is called F-N plot which is useful method to extract the electron effective mass in dielectric. When temperature is high enough for the electrons to overcome the energy barrier at the metal-dielectric interface and to be injected into the conduction band of dielectric by thermal energy, the conduction mechanism is changed to so-called Schottky emission, whose current density shows a positive correlation to temperature.

Hopping conduction and Poole-Frenkel emission

These two conduction mechanisms are categorized in bulk-limited conduction. Current is mediated by the defects that can trap charge with a lower barrier height than that of the direct charge injection to the conduction bands. The trapped charge carrier in the defect can be migrated by quantum tunneling or thermal emission, and can be trapped again by the neighbor defect. Hopping conduction means the defect-mediated conduction when the hopping is drived by quantum tunneling (Figure 1b), and Poole-Frenkel Emission decribes the transition between defects as a thermal emission (Figure 1c).

Although the chemical formula of the material is the same, the amount of intrinsic defects whose presence is inevitable varies according to the fabrication methods. Current density is a function of the defect density, because the probability of charge carrier hopping depends on the distance between the defects. The equation for hopping conduction is

$$J = qanv \exp\left[\frac{qaE}{kT} - \frac{E_a}{kT}\right] \quad (2)$$

where a is the mean hopping distance, n is the electron concentration, v is the frequency of thermal vibration of electrons at defect sites, and E_a is the activation energy for hopping between defect sites.

The relationship between current density and temperature of Poole-Frenkel emission shows similarity to that of hopping conduction, whose equation is

$$J = q\mu N_C E \; exp\left[\frac{-q(\phi_T - \sqrt{\frac{qE}{\pi\varepsilon_i\varepsilon_0}})}{kT}\right] \quad (3)$$

where μ is the mobility of electron in dielectric, N_C is the density of states in the conduction band, $q\phi_T$ is the defect energy level. There are relationship between ln(*J/E*) and $E^{1/2}$ for Poole-Frenkel emission, whereas hopping conduction shows linear relationship between ln(*J*) and *E*.

Ionic conduction

Ionic conduction is the flux of ionic species in dielectrics (Figure 1d). Usually, the ionic species is a contaminant during the fabrication process such as alkali and alkali earth metal cations.[24,25,49] When large electric field or high radiative energy is applied, chemical chain is locally destructed, and ions such as O^{2-} can be generated.[38] These ionic species are located in the chemical structure of dielectric materials, and the chemical structure is distorted locally to stabilize excess charge. There is an energy barrier between each ion trap site, so the equation describes this mechanism is similar to the one for hopping conduction.

$$J = J_0 exp\left[-\left(\frac{q\phi_B}{kT} - \frac{Eqd}{2kT}\right)\right] \quad (4)$$

where J_0 is the proportional constant, $q\phi_B$ is the barrier height of ion trap site, and *d* is the mean distance between each ion trap site.

2.2.2. Dielectric breakdown

In dielectric films, current is allowed under the electric field by the mechanisms mentioned in the previous section. However, due to the dynamicity of the dielectric material, it loses its insulating property over time, or by the strong external stress. This phenomenon is called dielectric breakdown. After dielectric breakdown happens, considerable increase in conductivity is observed, and usually the change in conductivity is irreversible.

Dielectric breakdown induced by electrical stress have been deeply understood for decades, and these effort contributed to the rapid progress in sophisticated electronic devices.[38,50–53] There are several physical models which successfully address the dielectric breakdown phenomena, however, the chemical nature of dielectric breakdown is still debatable. The ambiguity is resulted from its complex nature. Firstly, it happens at the localized area of dielectric material thus the in-situ analysis has been limited. However, analysis using in-situ and ex-situ electron microscopy have been conducted to elucidate the microscopic nature of dielectric breakdown recently, the chemical change around the breakdown spot was being revealed.[9,10,54] The second reason is its suddenness. Breakdown happens at unpredictable time, and the change in dielectric film is usually completed in an instant, thus the high temporal resolution is required.

Although the chemical nature is still unclear, the kinetics of dielectric breakdown is well understood based on statistical analysis. Varying electrical bias, temperature and thickness, the indicators of breakdown kinetics such as V_{db}, t_{db} and

Q_{db} were measured and analyzed. Breakdown models have been suggested to fit the statistical distribution of the indicators, and the brief introduction of them is presented below.

Briefly speaking, dielectric breakdown is an energy conversion process from applied electric potential energy to chemical rupture of the dielectrics.[38] The charge conduction of dielectrics starts with the electron injection to the conduction band of the dielectrics. The electron is then further accelerated and gains energy by the strong field. The energy of electron can be dissipated via various pathways, which drives the damage on the chemical structure of dielectric materials. Firstly, the electron loses its energy via scattering when they flow along the conduction band of the dielectrics. When they reach to the anode-side interface, the electron donates its energy to the surroundings during their relaxation to the fermi energy of the anode, and the energy can break the chemical bonds and induce breakdown. Or the transition energy generates electron hole pair at the anode side and the hole can be injected to the dielectric's conduction band, making secondary damage. Lastly, hydrogen species are major suspects which are responsible for SiO_2 breakdown.[18,55,56] In SiO_2, there can be hydrogen species in the bulk SiO_2 or the interface in forms of defects like silanol (SiOH) or hydrogen bridge.[57,58] The hydrogen species serve as the trap sites for electrons and holes which increase the conductivity of SiO_2. Moreover, the electrical energy induces these hydrogen species to release in form of atomic hydrogen, which is not only highly diffusible in SiO_2 but also chemically reactive to induce secondary chemical reaction that could change the structure of SiO_2 chain.

All the models mentioned above were suggested to address the possible converting pathway of electric potential energy to chemical energy that induces the destructive reaction for breakdown. Therefore the amount of charge that flows through the dielectric materials and the potential applied to the film are the most important factors which determine the breakdown for most cases, although it is hard to define the exact dielectric breakdown mechanism that actually fit for given experimental system. Conversely speaking, conduction through the dielectric materials can be indirectly evaluated by measuring dielectric breakdown kinetics, when the current is too small to be precisely measured.

2.2.3. Electrolyte/oxide/semiconductor (EOS) system

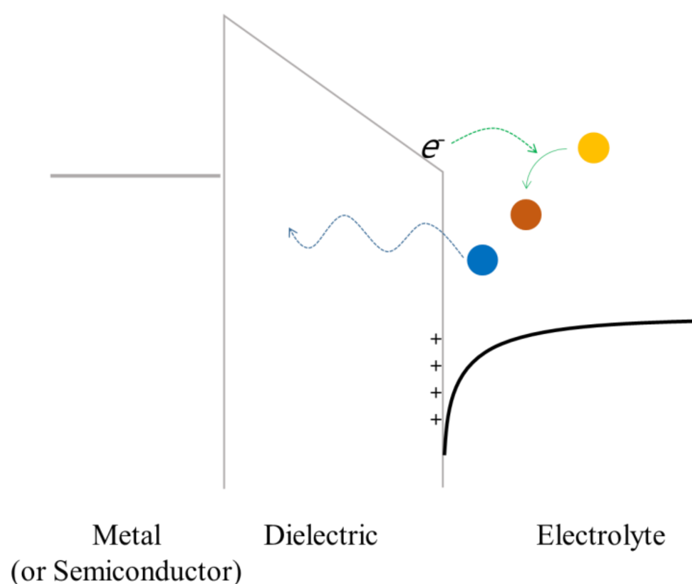

Figure 2. A schematic diagram of EOS system under cathodic bias.

When oxide-deposited electrode is immersed in electrolyte, which is named EOS systems, there are additional factors to be considered when compared to metal/oxide/semiconductor (MOS) systems. The schematic cartoon is presented in Figure 2 which represents the additional factors. The first one is the interface of oxide and electrolyte. In MOS system, the interface of metal and oxide defines the potential difference between the fermi level of metal and the bands of oxide. The interfacial potential is built according to the chemical nature of the interface.[36,59,60] However, the interface between oxide and electrolyte has more diversity according to the chemical environment of electrolyte. The ions in the electrolyte can modulate the surface potential of oxide, changing the net electrical potential difference between semiconductor and electrolyte.[61] The pH of electrolytes changes the

surface terminal group of the oxide by acid-base reaction. Ion sensitive field effect transistor (ISFET) is a kind of pH sensor where this principle is applied. The relationship between surface potential and pH is ideally Nernstian, however, the deviation is observed due to the wet oxide region and the adsorption of other species.[30,61–63]

The second factor that should be considered is the mass transport of chemical species between electrolyte and oxide. Mass transport is also possible in all-solid state devices, such as the alkali metal cation's diffusion[25,27,41] where the cations are introduced as contaminants during the fabrication process and Cu^{2+} diffusion from the anode side.[64] These metallic cation's diffusions have been regarded to be responsible for the performance degradation of devices since they shift the gate voltage. The presence of cations also weakens the dielectric strength of the oxide by enhancing the local electric field.[24,40] At the oxide-solution interface the concentration of the possible intercalating species is rich because alkali metal cations and protons are present in electrolyte. However, the role of these ionic species and their permeability in EOS system have not been experimentally examined precisely. In addition, the solvent molecules in the electrolyte phase sometimes can penetrate into the oxide matrix, developing wet oxide region near the interface. Especially for aqueous interface, the diffusion of water is typical in various glass materials.[30,32] These solvent molecules change the chemical nature of the oxide, modifying diffusion characteristics in the oxide.

The third factor is the charge transfer reaction at the oxide-electrolyte interface. When electrons are transferred from oxide to metal, the electrons are

injected to the empty states of the metal. Thus the charge transfer kinetics at the interface would rarely affect the overall conduction of MOS systems. However, the density of state of electrolyte is much lower than metal, thus the interfacial charge kinetics would cause significant difference in conductivity. Although the exact interfacial charge transfer reaction has not been revealed yet, there can be four kinds of electrochemical reactions expected at the interface. The first reaction is the reaction of adsorbates on the surface terminal groups. For example, surface adsorbed protons could be reduced. The second type of reaction is outer-sphere electron transfer to the redox species dissolved in electrolyte. Such molecules like ferrocene, ruthenium hexamine, electrochemically react very fast, thus the conduction would be increased. The third type would be the generation of solvated electrons.[65,66] Due to the large band gap of dielectric materials, the conduction band of them locates close to the vacuum level. The energy of electrons in the conduction band is large enough to generate the solvated electrons, which have great reducing power. Successive and unpredictable electrochemical reaction which cannot be expected at conventional electrodes would occur. The aforementioned three types of electrochemical reactions are conducted by electrons flow through the oxide dielectrics, however, the last type is about the electrochemical reaction of foreign species or defects in the oxides. Because the dielectric materials are in contact to electrolytes, the mass transport of chemical species from electrolytes to dielectrics would be possible. These foreign chemical species not only can serve as charge carriers, but also can generate intermediates by the electrochemical reaction of themselves. Lee et al. reported that the possibility of electrochemical reaction

mediated by hydrogen species which can transferrable in thermally grown SiO_2.[31] Because the nature of the oxide film is largely different from that of electrolyte, intermediate species which are highly unstable in conventional solvent could be stabilized in the chemical structure of dielectrics. Atomic hydrogen is suggested to be one of the possible intermediates in SiO_2 which can induce unique electrochemical reaction when it meets the reactant molecules in electrolyte. Some reactions with large overpotential such as CO_2 reduction and other electrocatalytic reactions are expected, if the generation of these intermediates is controlled.

The additional factors of EOS system are plausible in a qualitative manner, however, the detailed understanding has not been achieved. For instance, the acceleration of breakdown kinetics in acidic electrolyte was observed where the dielectric film placed in between electrolytes, although the exact mechanism which describes the acceleration was not clarified.[35,67] Previous researches regarding on ionic conduction in oxides have been mainly reported by solid state physics community and ISFET community. The reported diffusivity from literatures differs by a couple of order,[30] thus it is hard to tell whether the ion of interests can actually intercalate and diffuse in the dielectrics and resultantly make significant difference in conduction and breakdown kinetics. Especially, protons' role is debatable because there are numerous works which calculated the diffusivity and activation energy of proton hopping in SiO_2, but the diffusion of protons is insignificant in some experimental works.[36]

2.3. Experimental Section

2.3.1. Materials

Phosphate buffer solution (PBS) was made by mixing phosphoric acid (Daejung, Korea), KH_2PO_4 and K_2HPO_4 (99.9%) from Sigma-Aldrich. Hexaammineruthenium(III) chloride (98%) is purchased from Sigma-Aldrich. Highly doped n-type silicon wafer (arsenic-doped, <100>-oriented) with a resistivity as low as 0.005 Ω cm was obtained from STC (Japan). AZ9260 photoresist and MIF300 developer were purchased from Merck (USA).

2.3.2. Preparation of dielectric film-coated Si electrode

The 6-nm and 10-nm thick thermal SiO_2 film was prepared by the dry oxidation of the Si wafer in oxygen environment at 950 °C. Briefly, after the wafer was cleaned with a mixture of H_2SO_4 and H_2O_2, the native oxide was stripped by HF dipping. A 20-nm-thick thermal SiO_2 layer was produced at 850 °C in a furnace with dry O_2 blowing followed by HF wet etching. After repetitive cleaning, 10-nm-thick thermal SiO_2 layers were formed at 950 °C in a furnace with dry O_2 blowing. 10-nm thick Si_3N_4 was deposited by chemical vapor deposition.

2.3.3. Protective layer coatings on Si/SiO_2

To define the exposed SiO_2 area and reduce unwanted pinholes in the oxide film, successive coatings of alumina, photoresist and photolithography were performed as follows. 100 nm-thick alumina film was deposited on the whole

wafer of Si/SiO_2 by SNTEK sputter. AZ9260 photoresist was spin coated on the wafer at 6000 rpm for 30 s. Post bake was conducted at 110 °C for 1.5 min. Then the wafer was aligned under a pattern-designed chromium mask (50×50 μm^2), and exposed to UV lamp. Developing was conducted by immersing the wafer into AZ400K developer (AZ electronic materials) for 2 min. After judging whether the wafer was well developed by optical microscope, hard bake was conducted at 200 °C for 15 min. Etching of alumina was conducted in 50 °C, 85% phosphoric acid for 5 min.

2.3.4. Electrochemical characterization

To minimize mechanical stress, the whole wafer without a dicing process was used for all the electrochemical experiments. For the electrical connection to Si/SiO_2, the oxide layer on the back of the silicon wafer was removed by scratching with a diamond point pen by ~1 cm^2 and casting a droplet of 48 % hydrofluoric acid solution. This area was covered by gallium-indium eutectic (≥ 99.99 % trace metals basis from Sigma-Aldrich) and then attached by ~10-cm-long conductive adhesive tape. The tape was connected to the working electrode cable of the electrochemical analyzer (CHI660, CH Instrument, US). 3 μL of electrolyte were dropped onto an exposed SiO_2 area to form an electrochemical cell. Pt wire and Ag/AgCl reference electrode (3 M NaCl) with a double junction filled with the electrolyte of interest were employed as the counter and reference electrodes, respectively. All potentials in this paper are referenced to Ag/AgCl reference electrode (3 M NaCl). Linear sweep voltammetry (LSV) was carried out to see

characteristic dielectric breakdown behavior of Si/SiO_2. Potential at which dielectric breakdown occurs (V_{db}) was determined to the most positive potential allowing more than 10 nA during LSV.

2.3.5. Theoretical calculation

Total energy calculations were performed by using Vienna *ab initio* Simulation Package (VASP) based on density functional theory (DFT).[68] The generalized gradient approximation with the Perdew−Burke−Ernzerhof (PBE) functional were applied to treat the exchange-correlation energy.[69] DFT energy calculations were conducted spin-polarized with a kinetic energy cutoff of 800 eV. A 2×2×2 *k*-point grid based on Monkhorst–Pack scheme was used for energy calculation.[70] For describing SiO_2 system, a 2×2×2 supercell of α-cristobalite structure (space group: $P4_12_12$) was adopted and fully relaxed until the residual force was less than 0.2 eV/Å. We estimated the relative stability of various alkali metal ions in between two mediums. One is in the solution, and the other is in interstitial sites in SiO_2 structure. The relative stability, ΔE, can be expressed as:

$$\Delta E(x) = E_{x\ in\ SiO_2}(x) - E_{SiO_2} - \{E_{x\ in\ vacuum}(x) + E_{solvation}(x)\} \quad \ldots\ldots\ldots\ldots(5)$$

where x is a kind of alkali metal ion such as Li^+, Na^+, K^+, Rb^+ and Cs^+. To determine the most stable interstitial sites in SiO_2, we considered seven different interstitial sites generated from Voronoi analysis.[71]Subsequently, the lowest-DFT-energy structure was selected to estimate $E_{x\ in\ SiO_2}(x)$ that contains one alkali metal ion. Only the internal atomic positions were allowed to be relaxed while the lattice constants were fixed to those of the fully-relaxed SiO_2 structure when we

calculate $E_{x\ in\ SiO_2}(x)$. E_{SiO_2} is the DFT energy of 2×2×2 supercell of *α*-cristobalite structure. The energy of single alkali metal ion in the vacuum, $E_{x\ in\ vacuum}(x)$, was obtained from a 20×24×24 Å^3 tetragonal unit cell with one ion in the box. The energy of the single ion was corrected by using solvation energy, $E_{solvation}(x)$, to estimate the energy of ion in solvated states (Table S1). Ab initio molecular dynamics (AIMD) simulations were carried out by employing VASP based on Verlet algorithm.[72] The same structures which were used for calculating $E_{x\ in\ SiO_2}(x)$ were adopted for AIMD simulations except for the Cs^+-inserted SiO_2 case where the electronic energy could not be converged in AIMD calculation conditions. We used a *Γ*-point-only *k*-point grid and a cutoff energy of 400 eV in AIMD. The simulations were performed for 100 ps after an equilibrium step of 10 ps in the canonical (NVT) ensemble with a Nosé–Hoover thermostat.[73,74] All AIMD simulations were conducted at an elevated temperature of 1,800 K to facilitate the ionic motions.

2.4. Results

2.4.1. Electrochemical analysis of large-area dielectrics. Effect of unwanted damage and misunderstandings due to the inevitable defects

In this section, the general electrochemical characteristics when the area of EOS systems is large will be presented. The electrochemical current and the surface area of macroelectrode have linear relationship in general. That is why most electrochemists use current density as an important data for their research. However, when using dielectric material on the electrode, the surface area and the current would not follow the linear relationship. This non-linearity is originated from the inhomogeneous conduction pathway of dielectrics which are discussed in the previous section. Besides, pinholes which are the physically damaged regions offer additional current pathway by allowing the molecules in electrolytes to reach the bottom electrode. Thus the current flowed by a little number of pinholes can overwhelm the current passed by other conduction pathway.

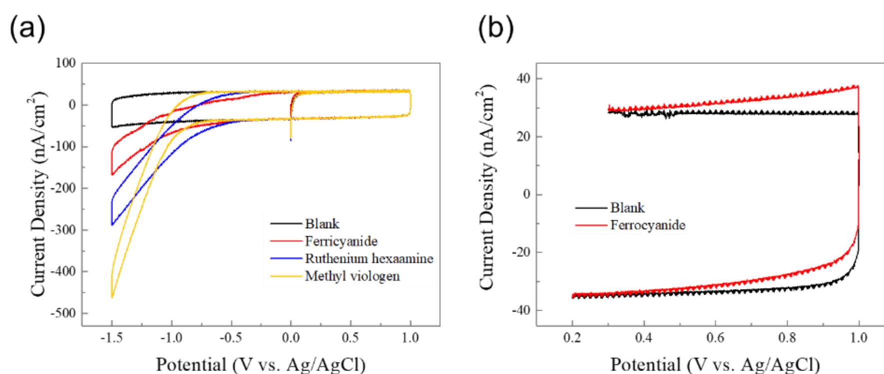

Figure 3. Cyclic voltammograms of Si/6 nm SiO_2 electrode at electrolytes containing (a) oxidized form of redox molecules and (b) a reduced form of redox specie.

A representative current-voltage relationship of 6 nm SiO_2/Si/buffered aqueous solution (pH7) is presented via cyclic voltammogram in Figure 3. It should be mentioned that the deviation of current is large by samples, thus the shape of the voltammogram will be discussed only. At the positive potential region, anodic current is observed when the reduced form of redox molecule, i.e. ferrocyanide is in the electrolyte (Figure 3b). When the electrode is pre-oxidized before measuring the ferrocyanide solution, the current is blocked. Thus it can be concluded that the electrode has some weak regions on it, and they can be cured by electrochemical oxidation at harsh oxidative potential. The cathodic current onset potential locates around -1 V vs. Ag/AgCl reference electrode. The cathodic current is also blocked by anodic curing, however it is much easier to flow cathodic current than to flow anodic current in terms of overpotential.

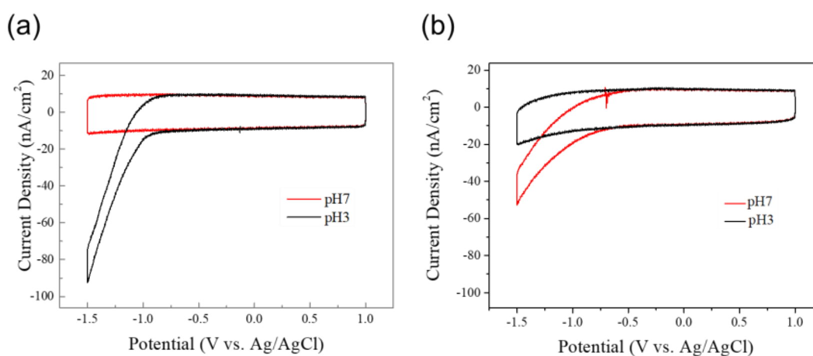

Figure 4. Cyclic voltammograms of Si/6 nm SiO_2 electrode conducted at the electrolyte containing (a) ferricyanide and (b) ruthenium hexamine (III) at different pH.

The cathodic current of uncured electrode is related to the electrolyte's pH and the redox molecules in the electrolyte. The current is increased when the oxidized form of redox species, i.e. ruthenium hexamine (III), ferricyanide and methyl viologen, is presented in Figure 4. The increase of current is affected by pH. When the charge of redox molecule is negative, the current is bigger at the lower pH, whereas the current is smaller at the lower pH when the redox molecule has positive charge. Thus the observed current would be affected by the electrostatic force between the surface of SiO_2 and the redox molecules.

However, it was found that the intrinsic conductivity of SiO_2-based EOS system could not be measured due to the pinholes or chemically weak spots on the electrode when the exposed area is large. Therefore, the strategies for minimizing the damaged area and ensuring the uniformity in the given exposed oxide surface

will be presented in the next section. The comparison of currents from the large area- and small area- electrode will be presented in section 2.4.3. and the intrinsic electrical behaviors will be discussed after then.

2.4.2. Methods for minimizing experimental deviation

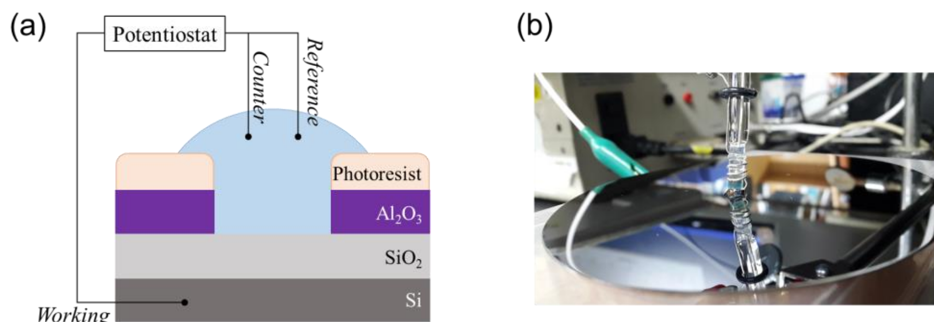

Figure 5. (a) A schematic diagram and (b) a photograph of the electrochemical cell for minimizing chemical and physical damage that possibly applied to SiO_2 layer. Alumina and photoresist define the exposed area of SiO_2 to be 50×50 μm^2. Whole silicon wafer serves as a working electrode to minimize unwanted physical damage during dicing or manual handling.

In this section, the strategies for preparing reliable electrode are presented. The damage in the dielectric oxide film would be categorized into two groups. The first one is physically damaged area due to the mechanical stress biased during the fabrication process. In this area, the film is thinner, or the underlying conductive surface is directly exposed to the electrolyte. The origin of physical damage would be sample handling or harsh mechanical process such as sawing. The second damaged area would be defect rich region, where the interband states lower the resistivity of the film. Thus the electrical response of chemical-defect-rich oxide is estimated to be thinner than real thickness. The defects are inevitably generated during the deposition process or during the exposure to the chemical such as

developer or etcher. Thus the film of interest should be minimally exposed to the chemicals.

When using the diced Si/SiO_2 or Si_3N_4 wafer without any protection method, the deviation of the electrochemical response was large. The origin of the large deviation was expected to be the defects and pinholes present in the exposed area. Generally, the number of physical and chemical defects in given surface area is proportional to the area, because the distribution of defects is random. If the area is smaller than the critical area, the possibility of an exceptionally weak area in the area is less than 1, so the smaller the area of the exposure, the smaller the deviation. When the area becomes so small a defect-free or a singular defect behavior can be observed.

Dicing is a useful tool for the ease of sample handling. However the physical and chemical damages are inescapable because the strain is applied by dicing saw and there are intense spraying of water during dicing. Thus dicing was avoided as long as possible for minimizing sample damage.

From these reasons, new strategies were adopted as follows (Figure 5). Firstly, additional protective film was deposited to prevent physical and chemical damages. A 100 nm-thick Al_2O_3 film was employed for this purpose, because its ease of etching in mild condition where SiO_2 and Si_3N_4 are hardly damaged. Secondly, photolithography was conducted to define the exposed area to be small. By reducing the exposed area to be hundreds of square micrometer, the physical defect is enough suppressed to analyze the conduction of intrinsic dielectric materials.

The etching of SiO_2 and Si_3N_4 when they are exposed to photoresist developer whose basic pH could possibly etch the dielectric films also can be prevented by Al_2O_3 layer. Al_2O_3 is also weak in basic pH, however, the thickness of the Al_2O_3 film is enough to stand and protect the SiO_2 for developing time. Lastly, the whole wafer was used without dicing to minimize physical damage. After taking these strategies, the electrochemical behavior of SiO_2 and Si_3N_4 was significantly changed as discussed in the following section

2.4.3. General electrochemical behavior of defect-suppressed dielectrics in contact to solution

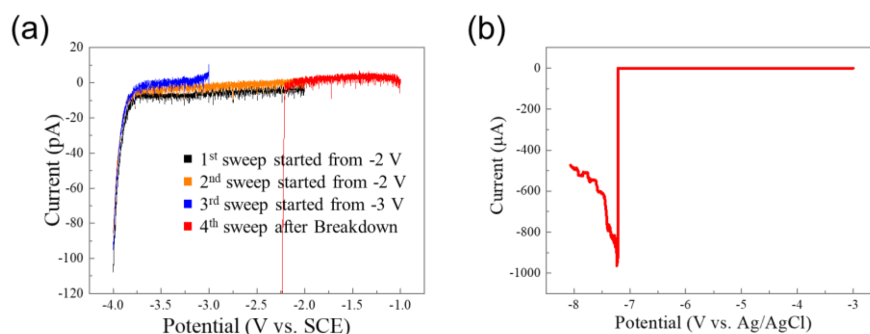

Figure 6. Cyclic voltammograms of area confined SiO_2 (50×50 μm^2) with the thickness of (a) 6 nm and (b) 10 nm.

A representative current-voltage characteristic of the Si/6 nm SiO_2/buffer electrochemical system measured in 0.1 M phosphate-buffered solution (PBS, pH 3) is shown in Figure 6. During the cathodic sweep, the current slightly or hardly increased before the explosive increment of current at ~−4 V was observed. The abrupt increase of current is a typical behavior of dielectric breakdown. Before the dielectric breakdown, slight current increase was observed, which reflect the tunneling current between electrode and electrolyte. A thicker, 10 nanometer-thick SiO_2 was formed by the same method as 6 nm SiO_2. V_{db} shifted to the more negative value of ~−7 V which was ~−4 V for 6 nm SiO_2. In the thicker oxide, no current increase before the dielectric breakdown is observed in the LSV which means the reduced tunneling probability between electrode and electrolyte.

When a large amount of charge injection was not allowed during preceding potential sweep by stopping the sweep manually, and conducted cathodic scan again, current-voltage behavior was very similar to the first one (orange curve in Figure 6a). To rule out the possibility of recovery of the dielectric property at the beginning of the cathodic sweep, the subsequent scan started as shown by the blue curve starting from -3 V, which resulted in similar voltammogram to the former ones. However, after the large current, whether by constant voltage stress or further voltage sweep (data not shown), the current-voltage relationship was permanently changed, implying that an irreversible chemical or physical change on the Si/SiO_2 electrode surface took place (red curve in Figure 6a). This cannot be explained by peeling-off of the oxide from the underlying conductive Si because the shape of the linear sweep voltammogram after breakdown is different from the voltammogram obtained when bare Si is directly exposed to the solution by HF chemical etching (data not shown). For the bare Si electrode, a hydrogen evolution reaction (HER) started to appear at a mild overpotential, −0.7 V. However, the cathodic current onset potential of Si/SiO_2 electrodes, which had experienced breakdown, is around −2.3 V. The sluggish HER will be discussed in the later section. The current-voltage response before the breakdown implies that the conducting pathway did not changed by the repetitive voltage sweeps. The number density of defects in the dielectric film is known to be increased under voltage stress,[38] however, the short-period voltage stress did not induce the defect creation.

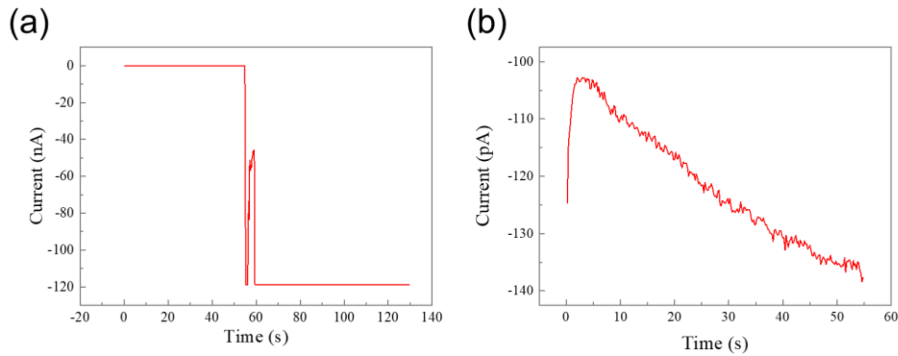

Figure 7. (a) A current-time curve of Si/6nm SiO_2 electrode under constant voltage (−4 V) stress and (b) its magnification of low current region.

A graph of time-dependent dielectric breakdown under constant voltage stress also showed a stepwise current increment (Figure 7a). A constant voltage stress, −4 V, induced the breakdown in the pH 3 buffer solution for the 6 nm-thick SiO_2 electrodes. Under the electrical bias, a small leakage current known as the stress-induced leakage current (SILC) was observed (the leakage current measured until 55 s is presented in Figure 7b). Unlike the current response during the voltage sweep, the increase in leakage current might result from the increase of the defect concentration. The number of defect is increased when the dielectric is exposed to an electrical stress by the chemical mechanisms as introduced in the previous section. Due to the increasing number of conduction pathways that comprise of defects, the resistance of the film is reduced in this period. After a sudden current rise, an indicator for the dielectric breakdown, the current kept increasing irregularly.

2.4.4. Cation effect on dielectric breakdown characteristics: sodium intercalation and accelerated breakdown kinetics

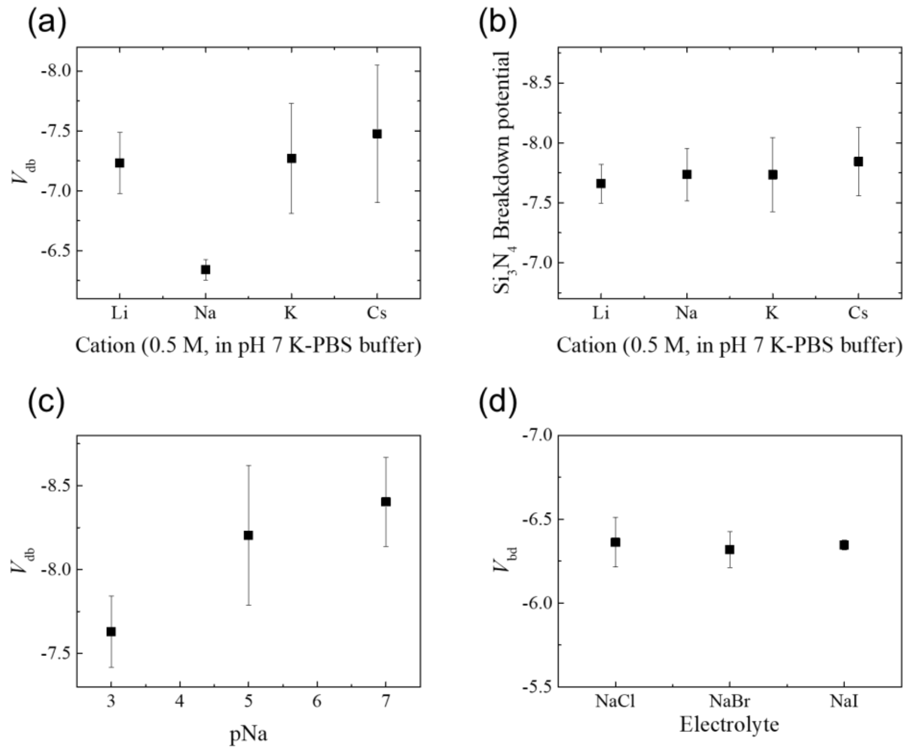

Figure 8. Breakdown potential (V_{db}) of Si/10 nm SiO_2 electrode obtained at the electrolytrytes varying (a) cations, (c) Na^+ concentration and (d) anions. Breakdown potential of Si_3N_4 with different cation is presented in (b)

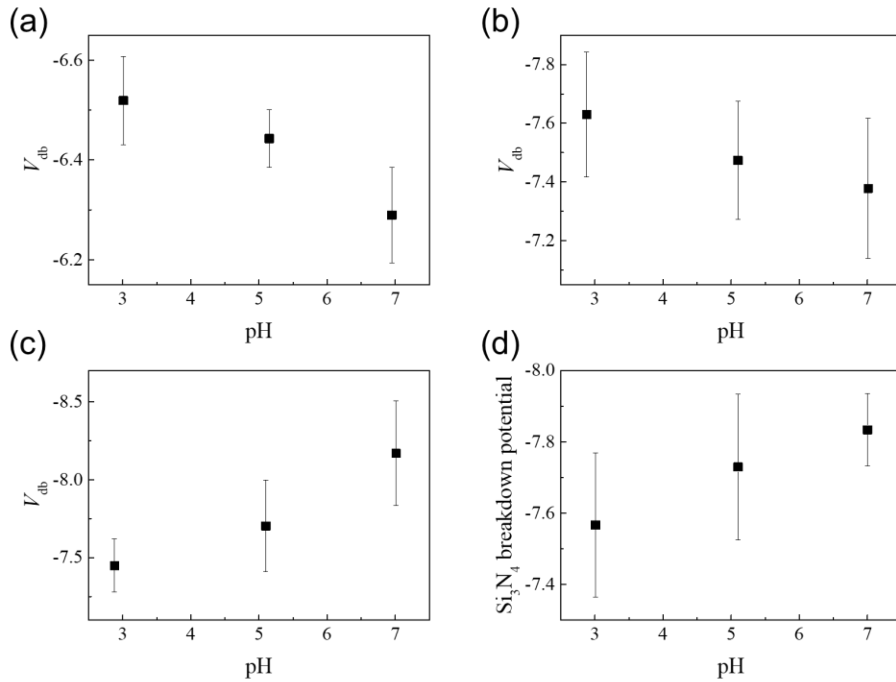

Figure 9. V_{db}-pH dependence of Si/10 nm SiO_2 electrode obtained at aqueous electrolytes containing (a) 0.5 M NaCl, (b) 1 mM NaCl, and (c) 0.5 M KCl. (d) V_{bd}-pH dependence of Si/10 nm Si_3N_4 electrode at aqueous buffer containing 0.5 M NaCl.

In this section, the effect of electrolyte will be discussed. The electrolytes containing 500 mM of alkali metal chloride salt buffered by 50 mM potassium phosphate buffer were used for the dielectric breakdown experiments in aqueous system. The effect of cations on dielectric breakdown potential (V_{db}) is presented in Figure 8. Among the alkali metal chloride solutions, only the solution containing NaCl affected the breakdown of SiO_2. V_{db} shifted positively when the solution contained sodium ions, and the deviation of V_{db} is reduced as well. Little changes

in V_{db} were observed with varying anions (Figure 8d). The effect of sodium cations on breakdown potential cannot be observed for the breakdown of Si_3N_4 (Figure 8b), which means the effect is originated from the chemical nature of the SiO_2. The sodium effect was enhanced with the increased sodium concentration, whose slope is −190 mV/pNa (Figure 8c).

According to the previous papers,[46] the pH of electrolyte significantly affects the kinetics of dielectric breakdown. They conducted the dielectric breakdown experiment of thin Si_3N_4 film of which the both sides make interfaces with electrolyte. When the pH of both electrolytes was identical, dielectric breakdown was faster at the more acidic electrolyte. If the pH of each side was different across the film, the faster dielectric breakdown was observed when the electrolyte of oxidative applied potential was more acidic than the electrolyte of reductive potential. From these observations, they suggested that the proton conduction in the film and interfacial charge transfer reaction in which protons are involved was the key factors to understand the dielectric breakdown phenomena in electrolyte-solid interface.

To confirm whether the effect of pH on the dielectric breakdown of SiO_2 in the Si/SiO_2/electrolyte system has the same tendency, we varied the pH for each electrolyte. V_{db} shifted positively with the decrease in pH of the electrolyte containing KCl (Figure 9c, −160 mV/pH), which was expectable from the previous reports. However, the inverted tendency was observed when the electrolyte contained Na^+, and the slope was ~59 mV/pH (Figure 9a and 9b). The tendency didn't change when the sodium concentration was reduced to 1 mM. For Si_3N_4 film,

the slope of −70 mV/pH was observed (Figure 9d).

The inverted tendency of V_{db} to pH when Na^+ is presented can be addressed by the surface charge changed by protonation. When Na^+ is transferred from aqueous phase to SiO_2, it would interact with the SiO_2 surface first. Because the charge of SiO_2 surface is changed according to the solution's pH, the degree of sodium transference would be affected by pH. At the acidic solution, the surface charge of SiO_2 becomes positive, which makes the mass transport of cation unfavorable.[63,75] The slope of V_{db} lowering versus pH when sodium cations are presented, −60 mV/pH, infers that mass transport of Na^+ is affected by surface potential built by protonation. On the other hand, when there is no cations that can transfer through the interface, breakdown occurs at lower potential at acidic solution. There are numerous studies reporting the proton conductivity of silica.[19,44,76,77] Thus, it is reasonable that protons could transport from solution phase to SiO_2, and then they lower V_{db}. However, the probability of proton transport into the dry SiO_2 matrix from the solution phase would be less persuasive considering the large hydration energy of protons and its slow diffusion in SiO_2.[30] Nevertheless, protons are still expected to penetrate inside the oxide because there are adsorbed protons on the surface and the sub-surface region in the form of silanol whose solvation shell is partially peeled off. The probability of proton intercalation is evidenced by the pH dependence of Si_3N_4 breakdown. When SiO_2 is substituted to Si_3N_4 film which is known to suppress electrolyte induced hysteresis in ISFET,[30] there are relatively weak correlation to pH, −70 mV/pH. As the protonation changes the effective bias applied on dielectric film by 59 mV/pH (Figure 9d), this correlation infers that the

protons hardly diffuse in Si_3N_4. On the other hand, SiO_2 has the stronger correlation between pH and V_{db}, thus the contribution of protons by mass transport would be highly reasonable, lowering the V_{db} by intercalation.

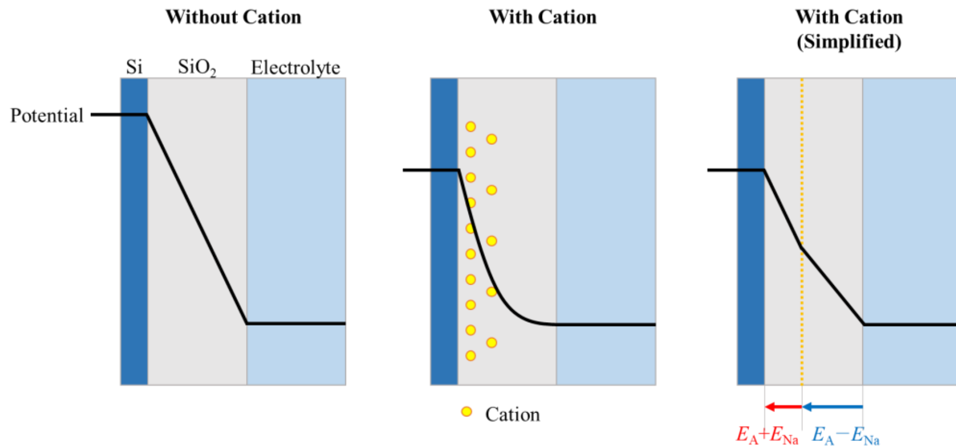

Figure 10. Expected potential gradient of EOS system (left) without and (middle, right) with cation species that can transport to SiO_2 from electrolyte.

The breakdown lowering ability of cation species can be found in the previous research of solid state device. They reported that V_{db} is lowered by mobile cations in dielectric films by increasing effective electric field in the film (Figure 10).[24,40] Like electric double layer built at the vicinity of electrode surface, mobile cations in the dielectric film accumulate near the Si/dielectric interface, steepening the potential gradient. Resultantly, the chance of electron injection to the conduction band of dielectric is increased by locally enhanced electric field, lowering V_{db}. In this system, it is expected that Na^+ could be transferred from the aqueous phase to the SiO_2 matrix.

With the same method that was used to calculate the number of cations introduced to hydrogenated silicon carbon nitride film in the literature,[40] we estimated the number of sodium ion in SiO_2. Briefly, assuming that the injected Na^+ is positioned on a plane, the effective electric field can be calculated simply from the sum of the applied field and the field generated by Na^+ ions (Figure 10c). The potential differences at Si-SiO_2 and SiO_2-electrolyte are not considered because the applied potential is significantly larger, so the magnitude of applied field E_A would be V_A/d, where V_A is applied potential between reference and Si and d is the oxide thickness. By the gauss law, electric field is made by sodium ion plane in the film with the magnitude of $E_{Na} = qN_{Na}/2\varepsilon$ where q is the charge of electron, N_{Na} is the area density of Na^+, ε is the permittivity of free space. Thus, the electric field applied between Si and Na^+ plane is $E_{total} = E_A + E_{Na} = V_A/d + qN_{Na}/2$. When E_{total} exceeds the dielectric strength of SiO_2, which is V_{db}/d without Na^+, breakdown would happen. Using the measured V_{db}, the estimated number of sodium ions per unit area of 10 nm-thick film is 1.26×10^{16} m^{-2}, one sodium ion per 3,000 SiO_2, or 20 mM.

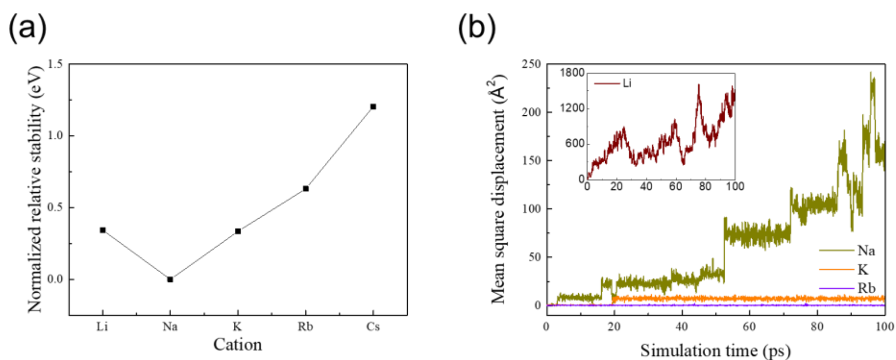

Figure 11. (a) Normalized free energy required to cation transport from aqueous to SiO_2 phase. (b) Mean displacement of cations versus time for different alkali metal cations calculated by molecular dynamic simulation.

The cations transportation between two different phases would be divided to 3 steps. (1) The solvation shell that stabilizes cations in solution phase should be peeled off completely or partially before the cations enter the oxide. (2) In the oxide, the lattice is distorted or locally reduced to stabilize the local excess charge. (3) On the interface, the adsorption of the cation on the terminal group of the oxide can catalyze the transport process by lowering activation energy. In order to further elucidate the cation selectivity of SiO_2/aqueous system, we conducted theoretical calculations based on DFT, by estimating the relative stability of alkali metal cations. In Figure 11a, the normalized relative stability of alkali metal cations in SiO_2 against in water is plotted as a function of the cation species. We normalized the values based on the minimum, specifically the value of Na^+, to present the effect of cation species clearly. The positive values for Li^+, K^+, Rb^+, and Cs^+ imply

that they have less preference for residing in SiO_2 matrix than Na^+, indicating that Na^+ ions have the highest driving force for the insertion from water to SiO_2. Nevertheless, it should be noted that the results do not demonstrate only Na can be inserted into SiO_2 structure. We also investigated transportability of alkali ions in SiO_2 structure by AIMD simulations. The calculated mean square displacement of each alkali ion is depicted in Figure 11b as a function of simulation time. It is observed that alkali ions bigger than Na^+ ion can barely migrate in SiO_2 matrix, implying that they are less likely to contribute the breakdown enhancement even if the cations intercalate into the first layer of the matrix. In contrast, the ionic motion of Li^+ shows much faster than others. Yet, it is expected that the role of Li^+ on V_{db} seems less significant than Na^+ because its insertion from water to SiO_2 is energetically less favorable than Na^+. The adsorption of alkali metal ions on SiO_2 surface is affected by the anions and strongest adsorption of Na^+ was made when Cl^- is presented,[61] however, no significant change in V_{db} experiment was observed (Figure 8d).

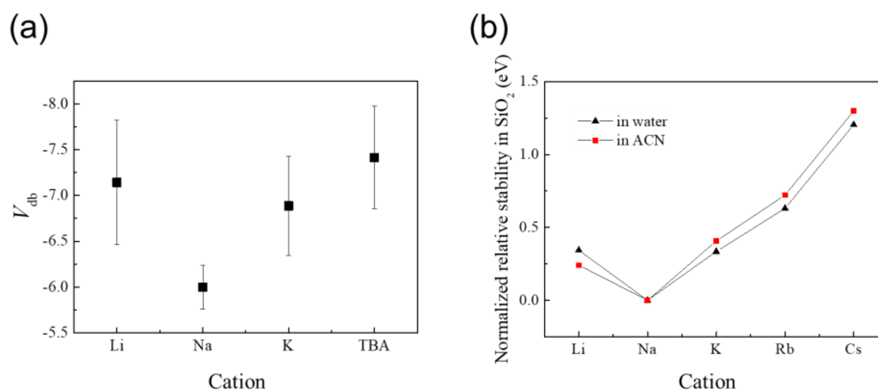

Figure 12. (a) V_{bd} of Si/10 nm SiO_2 electrode obtained at organic solvent (acetonitrile) based electrolyte containing 0.1 M of $LiClO_4$, $NaClO_4$, $TBAClO_4$ electrolytes. The saturated $KClO_4$ electrolyte was used due to its low solubility. (b) Calculated normalized relative stability of when alkali cation is transferred from acetonitrile to SiO_2. Data obtained from SiO_2-water system is also presented for comparison.

Because the solvation energy of each phase is important factors for the selectivity of ion intercalation, the assumption was made that the selectivity becomes different at other solvent environment. We modified the solvation energy by changing solvent to acetonitrile.[78] However, there are relatively small changes in the difference of solvation energy of cations between typical solvents, so in most cases the selectivity would not change significantly. (Figure 12)

Therefore, it can be concluded that protons play multiple role in the conduction of dielectric film. Firstly, surface protonation would affect the effective field applied to SiO_2 film, thus the electronic conduction and the ionic conduction

rate would be changed. pH modifies the potential difference by 59 mV/pH, so V_{db} would shift by 59 mV/pH for ideal dielectric material. When there are ions that can be transferred to dielectric material such as Na^+ into SiO_2, interfacial protonation interferes with the introduction of Na^+, making it difficult to cause dielectric breakdown. In the absence of transferrable species, the injection of the proton itself contributes to dielectric breakdown.

2.4.5. Electron scavenger effect on dielectric breakdown characteristics: non-destructive conducting pathway by electron scavenger

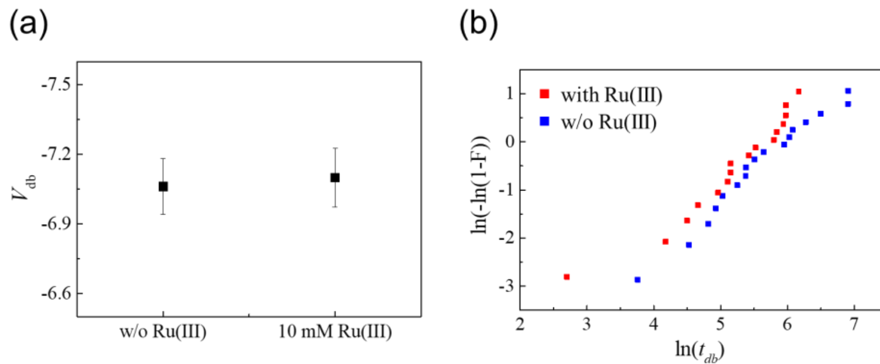

Figure 13. (a) V_{bd} and (b) Weibull plot of Si-SiO_2 Si/10 nm SiO_2 electrode broken down at aqueous electrolyte with or without 10 mM ruthenium hexamine (III) in 0.5 M KCl buffered by 50 mM phosphate buffered solution (pH 3).

In the literature reported by K.Briggs et. al., they suggested that the protons and hydroxides were the reactant for the charge transfer reactions which should occur at the electrolyte-oxide interface for charge balance. Thus the dielectric breakdown kinetics is accelerated when pH is lower at anode side. In this thesis, this assumption is generalized as follows; if the interfacial charge transfer reaction is facilitated by the chemical species in the electrolyte, the faster dielectric breakdown kinetics will be observed.

Ruthenium hexamine is a well-known redox species with a standard reduction potential of 0.1 V vs. NHE which is comparable to that of hydrogen evolution reaction that would most likely occur at the interface. If the assumption is correct, the presence of 10 mM ruthenium hexamine (III) will accelerate the dielectric breakdown because its reduction reaction to ruthenium hexamine (II) would be much faster than HER in pH3. However, both potential sweep- (Figure 13a) and constant potential- (Figure 13b) dielectric breakdown experiments show little difference by the presence of ruthenium hexamine (III). The time for breakdown, t_{db}, is analyzed by Weibull analysis which is a widely accepted statistical analysis for breakdown. According to the Weibull analysis, the probability of breakdown is increased over time, inferring that the breakdown kinetics is accelerated under voltage stress. The acceleration would be originated from the increasing concentration of defect in the dielectric film as shown in Figure 7b. t_{db} showed wide variations, from a couple of seconds to several hundreds of seconds. According to the percolation model, the large deviation of breakdown is a general characteristic of thin dielectric films. Although the deviation of t_{db} is large, the Weibull plot clearly shows the irrelevance of redox species to the breakdown kinetics.

The little effect of electron scavengers in solution phase refers to that charge transfer reaction at electrolyte-oxide interface is not a significant factor for dielectric breakdown. There are two possible reasons which could address this phenomenon. The first one is that the electron scavenger does not enhance the electron transfer rate at the oxide/electrolyte interface. When the conduction occurs

in dielectrics, electrons should be injected to the conduction band first. The electrical potential energy of electron in the conduction band of SiO_2 is high, which is only 0.9 eV lower than vacuum level. This high-energy electron should be ejected to the solution phase. We suspected that the reaction accompanying this charge flow would be the common electrochemical reactions of reducible species such as the reduction of proton or ruthenium hexamine. However, it can be deduced from the result that the charge imbalance in SiO_2 would be solved by other ways. We guess that the electrons in conduction band would be released in the form of solvated electrons.[66] The reactivity of solvated electron is strong, so they cause electrochemical reaction with not only protons or redox species, but also solvents nearby. Therefore, even though the redox species were ready to accept electrons, the effect was insignificant if the dominant reaction would be the reaction between solvated electrons and solvent molecules.

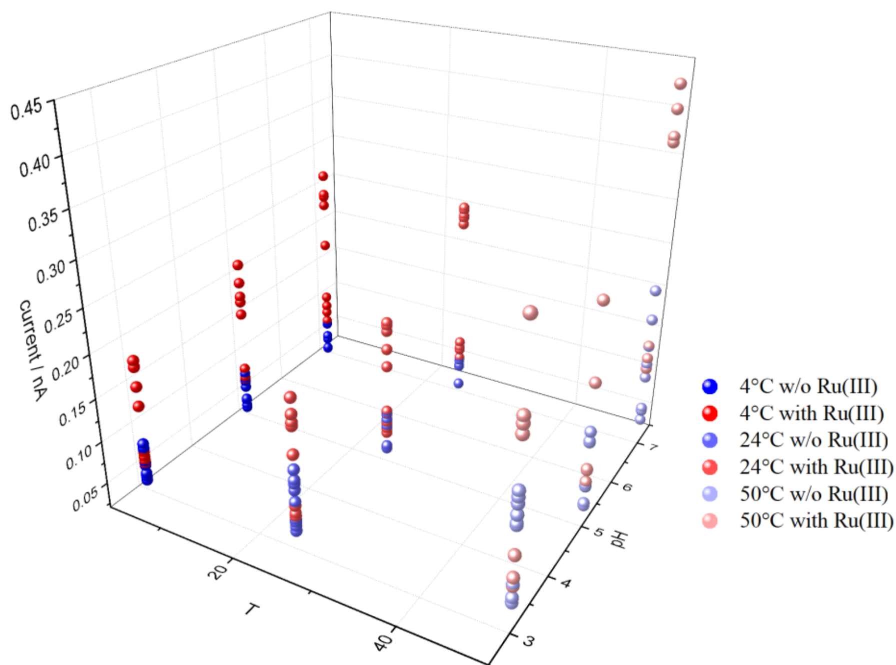

Figure 14. 3D-scatter plot of sampled current obtained at -7 V during negative potential sweep of Si/10 nm Si_3N_4 electrode varying temperature (x-axis) and pH (y-axis)

The second possible scenario is as follows. The presence of electron scavenger facilitates the charge transfer reaction at the interface, however the excess charge flowed in this pathway does not contribute to the acceleration of breakdown. To support this assumption, the Q_{db} of Si_3N_4 was analyzed. As shown in Figure 14, current is significantly increased when there is ruthenium hexamine (III) in the electrolyte. Thus, it seems that the electron scavengers facilitate the current flow in EOS system. The current attributed to redox species was affected by the potential profile of the double layer region, where the current is smaller at

the lower pH due to the coulombic repulsion of oxide surface and redox molecules. This is the third role of protons for the conduction of EOS system.

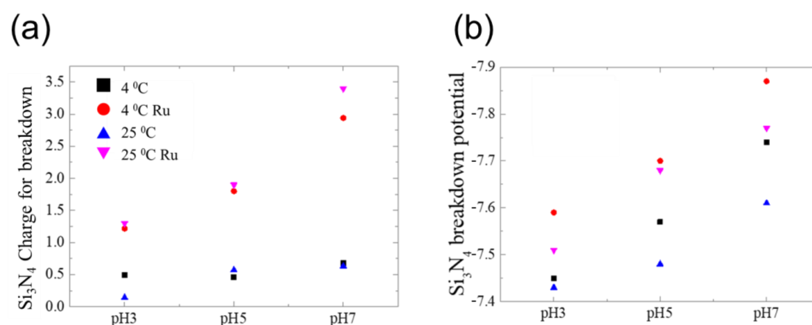

Figure 15. (a) Mean flowed charge until breakdown during the potential sweep at each condition. (b) Mean breakdown potential measured at each condition.

Analyzing Q_{db} offers the additional information of breakdown nature. Figure 15a presents the Q_{db} under various experimental conditions. It is shown that the bigger amount of charge is allowed in the presence of ruthenium hexamine (III). Interestingly, Q_{db} shows drastic change at the presence of electron scavenger when the pH of the electrolyte is varied. However, the little increase in Q_{db} at the lower pH was observed in the absence of ruthenium hexamine (III). V_{db} shifted to the positive potential at the lower pH with the slope closed to 60 mV/pH. The breakdown of EOS system containing ruthenium hexamine requires slightly more harsh potential compared to the system without ruthenium hexamine.

Thus the contribution of electron scavenger to the observed conductivity of EOS system is confirmed to be significant. However, the little effect of electron

scavengers on dielectric breakdown refers to that the observed charge transfer rate at electrolyte-oxide interface could not simply become an indicator for dielectric breakdown kinetics. Dielectric breakdown is originated from the electrochemical decomposition of molecular chain of insulator due to the charge carrier with high energy. Especially, the injection of hole and the release of hydrogen from the anode side are the main culprits responsible for dielectric breakdown. In solid state devices, the generation of these reactive species is known to be followed by electron transfer from the conduction band of insulator to the unoccupied state of anode. Thus the dielectric breakdown kinetics is accelerated at the condition of higher measured current. When the one side of the insulator is substituted with solution phase, however, two types of interfacial electrochemical reaction which have different contribution to dielectric breakdown seem to exist. Electrochemical reaction of non-adsorbate as in case of ruthenium hexamine (III) seems to have negligible contribution to dielectric breakdown, which means that this type of reaction would not drive hole injection or hydrogen release. Instead, the generation of hole and hydrogen would be attributed to the electrochemical reaction of surface states such as –Si-OH or $–(SiOH_2)^+$ at the surface of SiO_2. Electron scavenger in electrolyte would draw the high-energy electrons before they trapped to the surface state and make destructive species.[79] Consequentially, dielectric breakdown kinetics is unaffected in spite of the bigger current.

2.4.6. Post-breakdown phenomena

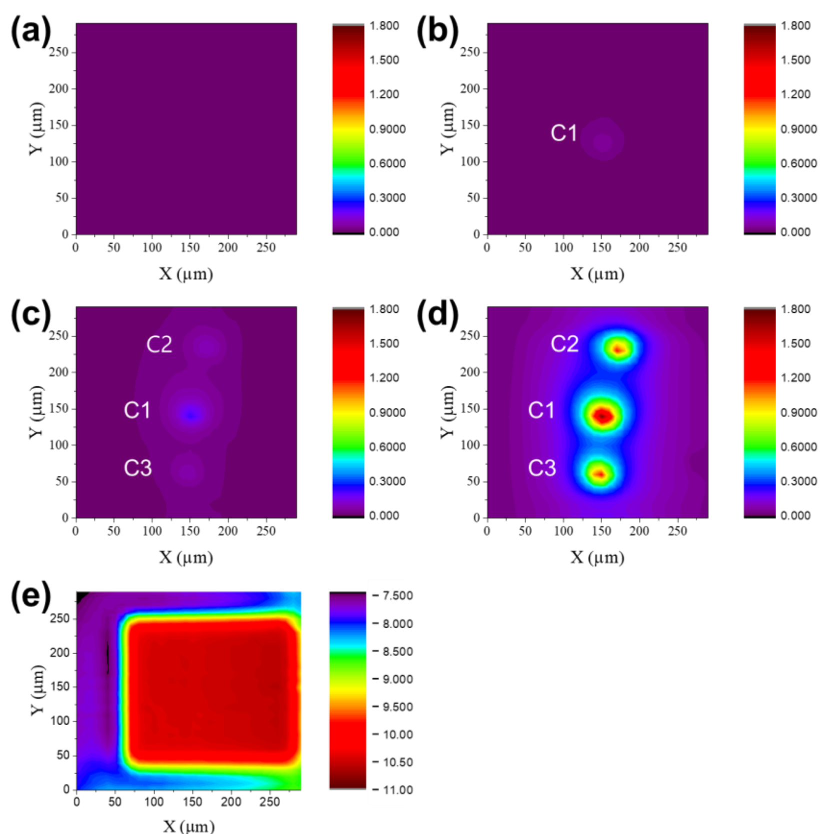

Figure 16. SECM images for a 200×200 μm^2 Si/6 nm SiO_2 substrate electrode obtained in a SG-TC mode, monitoring the $[Ru(NH_3)_6]^{2+}$ oxidation current of a tip with a tip potential (E_{tip}) held at −0.5 V in 10 mM $[Ru(NH_3)_6]Cl_3$/0.1 M PBS (pH 3) applying −1 V to the Si/SiO_2 substrate. Distance of tip to substrate is 10 μm. Scan rate is 50 μm s^{-1}. The unit of tip current is nA. (a) Before breakdown and (b) right after breakdown at −4 V in 0.1 M PBS (pH 3). After additional (c) 750-s and (d) 800-s voltage of −4 V application to the Si/SiO_2 substrate of (b) in 0.1 M PBS. (e) A SECM image for 200×200 μm^2 Si/SiO_2 substrate electrode obtained in a normal feedback mode, monitoring the $[Ru(NH_3)_6]^{3+}$ reduction current of a tip with a tip potential (E_{tip}) held at −0.5 V (vs. SCE) in 10 mM $[Ru(NH_3)_6]Cl_3$ dissolved in 0.1 M PBS (pH 3) without applying any potential to the Si/SiO_2 substrate. Distance of tip to substrate = 10 μm. Scan rate = 50 μm s−1. The tip current scale is nA.

According to the literature dealing with solid electronics, the breakdown of various oxide materials is generally known to occur locally at a relatively weak region of the oxide, whose exact physical and chemical features are still under debate.[10] SECM results show the similar characteristics to the previous literature from solid electronics. A SECM image of 6 nm-SiO_2/Si substrate electrode obtained in a normal feedback mode confirms the smooth substrate surface, without any physical defects (Figure 16e). For this 200×200 μm^2 Si/SiO_2 area, SECM substrate generation-tip collection (SG-TC) images were obtained in 10 mM $[Ru(NH_3)_6]Cl_3$/PBS solution (pH 3) before and after breakdown (Figure 15). The images are displaying tip currents with E_{tip} = +0.1 V, when $[Ru(NH_3)_6]^{2+}$ generated at the substrate with E_{sub} = −1 V can be collected and re-oxidized. As shown in Figure 16b, a local conduction spot is generated after breakdown, denoted as C1, around which a large tip current flows. COMSOL simulation tells that a tip electrode (10 μm dia.) can collect ~56.17 % of products generated from disk-shaped sources (~100 nm dia. and 2.5 μm dia.) located at a distance of 10 μm. Assuming the conduction spot to be a disk-type ultramicroelectrode (UME), its size could be inferred from the current using equation (2).

$$i_{\lim} = 4nFDCa \qquad (6)$$

where i_{lim} is the measured limiting current value, n is the number of electrons, F is the Faraday constant, D is the diffusion coefficient of $[Ru(NH_3)_6]^{2+}$ (9.12×10^{-6} $cm^2\ s^{-1}$, calculated from the literature), C is the concentration of $[Ru(NH_3)_6]Cl_3$, and a is the radius of the electrode. The greatest tip current measured was ~55.5 pA,

corresponding to 56.14 nm in diameter. To investigate the change of the conduction spot and Si/SiO_2 during the breakdown process, −4 V was further applied to the same substrate in PBS solution. After the further voltage application for 750 s, two more conduction spots (C2 and C3) appeared, while the size of C1 increased by 4 times (226.6 nm in dia.) (Figure 16c). With the assumption of a disk-shape conduction spot, the local conduction spot sizes of C2 and C3 are estimated to be ~83.56 and ~102.5 nm in diameter, respectively. Another 50 s with −4 V application to the same substrate produced no additional conduction spots, but the tip collection currents increased greatly, indicating widening of the local conduction spots previously created: 1.75 nA (1.770 μm in dia.) for C1, 1.21 nA (1.224 μm in dia.) for C2, and 1.20 nA (1.214 μm in dia.) for C3 (Figure 16d). According to these results, it is expected that a generated conduction zone becomes larger along with continuous charge flow to the substrate at −4 V.

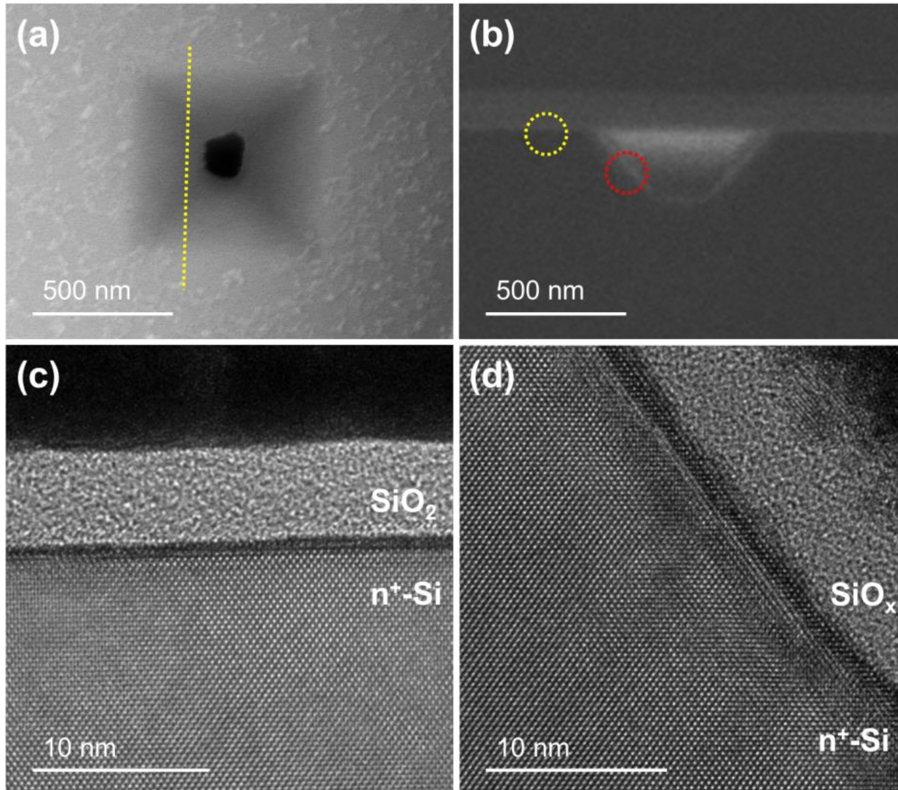

Figure 17. Representative SEM and TEM images of the inverted pyramid structure resulted from cathodic breakdown and post breakdown etching. SEM images of (a) top-view and (b) cross-sectional-side-view of the yellow dotted line in (a). Cross sectional TEM image of (c) undamaged Si(100) surface (yellow-dotted circle in (b)) and (d) sidewall of the inverted pyramid structure which has Si(111) surface with many steps (red-dotted circle in (b)).

The morphology of the conduction spots is like an inverted pyramid structure as shown in Figure 17. The angle between the sidewalls and the {100} surface of the wafer is 55° (Figure 17b), suggesting that the newly generated crystalline surfaces are Si{111} (Figure 17b). TEM analysis shows that the {111} sidewall is atomically rough with many steps (Figure 17d), whereas undamaged Si(100) surface is atomically smooth (Figure 17c).

Post-breakdown damages are often explained by Joule-heating of the local conduction path of the oxide because of large current through very narrow percolation path. In our experiment, however, the inverted pyramid structure seems to be created by the dissolution reaction of Si as indicated by the flat-etched crystalline surface. The possibility of the dissolution is supported by the oxide film which partially covers the dissolved region (Figure 17a). In contrast to the immense research effort focused on anodic dissolution, a few papers reported cathodic dissolution of Si. According to these reports, cathodic dissolution occurs when the cathode is much smaller than the anode, in a humid atmosphere, under tens to hundreds of volts as an external stress. They suggest that cathodic dissolution is originated from the pH increase which results from the HER near the cathode. According to our results in this study, the initial area of the conduction spot, a cluster of defects, should be very small, probably on the sub-nanometer scale. Electron transfer through this conduction spot and the local pH increase due to HER around it trigger the dissolution of underlying Si. It is no wonder that larger conduction zone leads to more vigorous HER, thus the thin oxide film over the conduction region could not hold out against rapid HER.

As aforementioned, a sluggish HER rate is characteristic electrochemical behavior at the conduction spots. HER requires a higher overpotential at the conduction spots than at the Si electrode covered with native oxide. The suppressed HER can be ascribed to the {111} surface of the sidewalls. At the cathodic potential, hydrogen atoms terminate the Si surface. We surmise that the Si{111} could be generated in our cathodic etching condition because it forms a stable hydrogen-terminated surface than other crystalline surfaces. Referring to the literature,[80] the {111} surface forms the most stable hydrogen-terminated surface among the crystalline surfaces of Si. The energy required for complete removal of 1 ML of hydrogen atoms from the hydrogen terminated Si {111} surface is 1.15 J m^{-2}, which is greater than the 1.04 J m^{-2} required for the {100} surface. In addition, the {100} surface has a less stable, 2 ML dihydride configuration compared to the 4/3 ML and the 1 ML surface. Therefore, HER at the {100} surface passivated with 2 ML hydrogen would be thermodynamically favorable. In conclusion, the sluggish HER at −1 V after the breakdown and the following cathodic etching might result from the stable hydrogen terminated surface of the newly generated crystalline sidewalls.

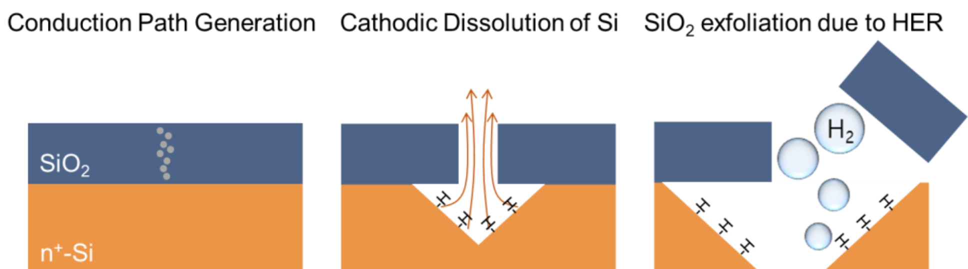

Figure 18. A schematic of Si/SiO_2 breakdown mechanism in acidic condition.

Based on our findings, a breakdown and post-breakdown mechanism of Si/SiO_2 in acidic conditions is proposed, as shown in Figure 18. First, defects are generated by applying a cathodic potential and thereafter the conduction path connecting the Si and the solution, which was described as a conduction spot, is created within the SiO_2 film. Second, cathodic dissolution of Si occurs as HER on Si induces augmentation of local pH; meanwhile, the exposed Si {111} surface is terminated by hydrogen. Finally, vigorous HER peels off the covering SiO_2 film, leading to an inverted-pyramid-shaped breakdown spot.

2.5. Summary

In chapter 2, the electrical conduction and the breakdown of EOS systems consisting of SiO_2 and Si_3N_4 as dielectrics were discussed. The current-voltage relationship of large-area-exposed EOS systems shows diode like behavior, which were previously interpreted as an evidence of hydrogen atom mediated electrochemical reaction. However, when the exposed area was shrunk, the voltammogram followed the typical behavior of dielectric breakdown. Therefore, the possible electrochemical pathway of hydrogen is not allowed by the bulk property of SiO_2, but allowed by the local chemical nature of SiO_2 which is expected to be the weaker region of oxide.

For the dielectrics where the number of weak spots is suppressed enough to conduct experiments for understanding bulk characteristics of dielectrics, the role of chemical species in electrolyte phase for the conduction of EOS systems is revealed. Firstly, Na^+ is transferrable to SiO_2 and reduces the dielectric strength, whereas other cations cannot. This is explained by the thermodynamic selection rule of alkali metal transfer from liquid phase to SiO_2. The selectivity measured in the aqueous solution would be valid for other solvent, because the hydration energy of alkali metals is largely split for common solvents.

Protons in electrolyte have multiple roles for the conduction of EOS system by modifying the surface potential built on the oxide/electrolyte interface. Firstly, they changes the barrier height for the mass transport of various charged species.

The shift of V_{db} by pH in Na^+ containing electrolytes shows that the barrier height is changed following Nernstian trend. Protons also gate the approach of redox species to the oxide/electrolyte interface or underlying electrolyte via changing the potential gradient near the interface and pinholes. Thus the conduction is affected by the pH of the electrolyte in the presence of redox molecules. Secondly, the generation of surface potential changes the net potential applied to the oxide in EOS systems, which shift the observed V_{db}. Lastly, protons can intercalate into the dielectric matrix. Although there are some reports that the diffusion of protons is limited in the sub-oxide region near the electrolyte due to the slow diffusivity of proton compared to the diffusivity of alkali metals, the diffusion of protons in SiO_2 is ascertained by the off-nernstian slope of pH-V_{db} plot obtained at K^+ based electrolyte.

Lastly, the role of redox species in the conduction of EOS system is intuitive in terms of conductivity. It lowers the charge transfer resistance at the oxide/electrolyte interface. However, the increase in conductivity did not accompany the acceleration of dielectric breakdown. Thus it seems that the conduction mediated via the outer sphere electron transfer reaction at oxide/electrolyte interface hardly generates the destructive species such as atomic hydrogen and hole. Therefore, the breakdown of EOS system would be attributed to the interfacial electrochemical reaction of surface adsorbed species.

Based on our findings, the reported breakdown kinetics from other researchers can be explained clearly. Considering that the penetration of protons was

irresponsible for the breakdown of Si_3N_4 in this work, the argument in the previous literatures which addresses the enhanced breakdown kinetics at acidic environment as an ionic conduction of protons seems to be less convincing. Instead, the pH of electrolyte not only changes the surface concentration of surface-adsorbed reactants for electrochemical reaction, but also modifies the net electric field applied to the oxide, changing the observed breakdown kinetics. It was confirmed that not every conduction pathway contributes the dielectric breakdown. The outer-sphere pathway reduces the resistance at oxide/electrolyte interface, but the increasing current doesn't change the observed behavior of dielectric breakdown.

In addition, these findings are expected to contribute to the deeper understanding of EOS systems failure. For the advanced performance, the devices incorporating EOS system employ thinner dielectrics. The dielectrics are supposed to be exposed to high electric field stress under operation condition, which have similar condition with this work. Although this study deals only with SiO_2 and Si_3N_4, further analysis of other dielectric materials can provide useful criteria for material selection in EOS device implementations.

3. Full-color-tunable Electrochromic Device Using Tungsten Trioxide Thin Film

3.1. Introduction: Electrochromic Device and Nanostructure for Better Optical Performance

Ion conductive oxides generally show unique changes in material property when the ions are intercalated. Electrical and optical property can be easily and reversibly modulated by applying electrical energy because the ion intercalation changes the electronic structure of the material. This switchable characteristic expands the possible application fields to the various devices such as electrochemical gating field effect transistors, electrochromic devices, etc.

Among the application fields, electrochromism utilizes the change in optical property. The reflectance and transmittance can be modulated, and researches are being conducted to construct efficient optical products such as electronic paper, smart glass and the electrochromic dye for the indicator of sensor. Numerous works have been reported which exploited various oxide materials such as VO_2, WO_3 and NiO_2, and polymers.

Tungsten trioxide (WO_3) is not only a well-known electrochromic material, but also a candidate for the anode of the lithium-ion (Li) battery of the next generation due to its electron conductivity and ionic capacity, which operates in

mixed-conduction mode.[14,81] In particular, optical tuning with WO_3 has been studied for decades as a potential candidate to implement electronic paper, since the color of the WO_3 immersed in electrolyte containing H^+, Li^+ or Na^+ changes largely from transparent (pale yellow) to dark (deep blue) by the intercalation of cations. To my knowledge, most devices have used WO_3 films of micrometric thickness for the sufficient color change,[3] resulting in the range of application to be restricted due to their unique monochromatic color adjustment.

The light tunability in the wide frequency domain from visible to far IR is one of the great opportunities that nanophotonics can offer. After the generation of color was achieved by means of plasmonic nanostructures or metasurfaces with well-designed structure,[82–85] significant efforts have been made towards the tuning of the spectrum in the visible with diverse physical and chemical mechanisms such as the modulation enabled with liquid crystal, reversible electrodeposition,[86,87] electrochromism,[88,89] chemical catalysis,[90] and the Purcell effect.[91] However, all these techniques still cannot meet the requirements for commercial display due to the difficulties in improving the purity of color, expanding the range of colors and manufacturing large areas from unavoidably complicated configurations.

Electrochromism have been suggested as a possible strategy to enable the tunability to nanophotonic deivices. Given that apparent but monochromic color tuning of WO_3, nanophotonics seems to be able to synergistically combine with WO_3. However, dynamic light tuning of nanophotonic device using WO_3 has not reported yet.

Therefore, in this chapter, electrically adjustable color devices based on WO_3 thin film are demonstrated. Strategic approaches are provided to generate various color and high-contrast color tuning with simple structures which do not require tricky fabrication techniques. Large frequency shift and intensity modification observed by reflective and transmissive type devices are presented and their performance is evaluated.

3.2. Experimental Section

3.2.1. Reagent and Appartus

WO_3, $LiClO_4$, $AgNO_3$, and gallium-indium eutectic (≥99.99% trace metals basis) purchased from Sigma Aldrich (US), acetonitrile purchased from Daejung (Korea), were used without further purification. WO_3 was deposited by homemade radiofrequency magnetron sputter. Electrochemical analysis was conducted with commercial electrochemical analyzer, Reference 600 (Gamry, US). For *ex-situ* and *in-situ* optical measurement under potential bias, mobile potentiostat, Compactstat (Ivium Technologies, The Netherlands), was employed. Optical analysis was conducted with Cary 60 uv-vis spectromer (Cary, US), V-VASE spectroscopic ellipsometer system (J. A. Woollam, US), homemade optical analyzer incorporating Acton SP2300 spectromer, PIXIS 1300B CCD (Princeton Instrument, US) and 10500 solar simulator (ABET, US). Photolithography was conducted with MDA-400s mask aligner (Midas System, Korea) and Hexamethyldisilazane (HMDS; Clariant, Switzerland), AZ5214 and AZ 300 MIF (Merck, US) as chemical reagents.

3.2.2. Deposition of WO_3 films

The WO_3 sputter target was made with WO_3 powder. The WO_3 powder was placed on Cu back plate and pressed with ~6.5 Mpa pressure. The base pressure in the sputter chamber was set to below 1×10^{-5} Torr. The partial pressure during sputtering was set to 7 mTorr for Ar and 1.3 mTorr for O_2. RF power was 100 W. The distance between target and substrate was varied with substrate materials to

protect the substrate from a possible damage. The distance was 10 cm for Si substrate and 14 cm for Ag substrate.

3.2.3. Preparing WO_3 coated Si electrode for optical and electrochemical analysis

Firstly, the deposition rate of WO_3 on Si substrate under the given sputtering condition was found. The thickness of WO_3 film was extracted from the ellipsometry result whose detailed method is presented in section 3.2.5. The deposition rate was 3.4 nm/min. The thickness of the samples used for understanding the electrochemical behavior and the optical property of WO_3 film was 92 nm.

3.2.4. Electrochemical analysis

The electrochemical experiment was conducted by employing three-electrode cell with an Ag quasi reference electrode (Ag wire in 10 mM $AgNO_3$ and 100 mM $LiClO_4$ dissolved in acetonitrile) and a Pt plate as a counter electrode. 100 mM of $LiClO_4$ in acetonitrile solvent was used for electrolyte. For electrical contact of WO_3/Si electrode, the backside of Si was scratched by diamond point pen, and gallium-indium eutectic was applied to the scratched region. Finally a 10-cm-long conductive adhesive tape was attached on the gallium-indium eutectic. For galvanostatic intermittent titration experiment, −1.78 mA/cm^2 was applied to intercalate Li^+ for 5 s, and then system was rested in open circuit condition for 55 s to achieve steady state potential. Cyclic voltammogram was obtained with varying

scan rate from 5 to 500 mV/s.

3.2.5 Optical analysis

Optical analysis to find out the *n* and *k* was carried out with V-VASE spectroscopic ellipsometer system (J. A. Woollam, US) at the wavelength region from 400 to 800 nm. The transmisstion and absorption of WO_3 film was measured with Cary 60 uv-vis spectromer (Cary, US), and homemade optical analyzer incorporating Acton SP2300 spectromer and PIXIS 1300B CCD (Princeton Instrument, US) and 10500 solar simulator (ABET, US).

3.2.6. Fabrication of reflective- and transmissive- type device

Reflective type device has the simple structure of WO_3/Si which was used for understanding the property of WO_3 film. For the color of red, green, and blue, the 165, 230, 205 nanometer-thick WO_3 films were deposited, respectively.

For the device of transmissive type, a 40 nanometer-thick Ag film was deposited on ITO coated glass with the deposition rate of 0.1 nm/s. Then the atomic layer deposition of Al_2O_3 (30 cycles) was conducted to prevent the sputtering damage. WO_3 with the thickness of 100, 70 and 48 nm was deposited for red, green and blue device, respectively. Finally, 40 nanometer-thick Ag film was deposited again.

Photolithography was conducted to reduce the area of transmissive type devices. After thorough rinsing with acetone and isopropanol, samples were dried by N_2 blowing followed by dehyadration for 5 min on 150 °C hotplate.

Hexamethyldisilazane was spincoated (4000 rpm, 30 s) and baked for 3 min at 120 °C. AZ5214 photoresist was spincoated at 4000 rpm for 30 s, and softbake was conducted at 100 °C. After UV exposure (4 s, 15 mW/cm^2) with MDA-400s mask aligner, developing was conducted by immersing the wafer into AZ300MIF developer for 40 s. Finally Ar ion beam milling was conducted for 1 min to partially remove the top Ag film.

3.3. Results and discussion

3.3.1. Analysis on tungsten trioxide thin film

The ionic conductivity of WO_3 is originated from their ReO_3-type structure (empty perovskite). It has pores and voids between corner-sharing WO_3-octahedras, and the ion intercalation are possible by the following reaction.

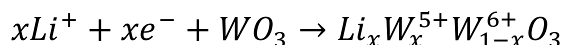

$$xLi^+ + xe^- + WO_3 \rightarrow Li_xW_x^{5+}W_{1-x}^{6+}O_3$$

The change in crystalline structure was reported during the charging and discharging. At lower charged state ($x < 0$), cations intercalate without changing monoclinic WO_3 structure. Then it is changed to orthorhombic, tetragonal, and cubic structure together with the increase of x. Not only the crystal structure, but also the electronic conductivity is changed along with the charging state: insulator to semiconductor ($x = 0.25$), and semiconductor to metal ($x = 0.4$).

In this work, the WO_3 film is used without further thermal annealing after sputtering. Therefore, it is expected that the WO_3 has amorphous structure which allow faster Li^+ diffusion compared to crystal phase. The WO_3 film is deposited on highly doped n-Si substrate for electrochemical and optical analysis due to its flatness and high conductivity. Before the electrochemical analysis, potential was cycled from 1 V to −1.5 V for making electrical connection between the WO_3 film and the underlying Si electrode because SiO_x layer generated during sputtering act as an electrical barrier. Oxygen supply is necessary to make oxygen-saturated WO_3

film, however, it induce thin dielectric SiO_x between WO_3 and Si. After several CV cycles, voltammograms became indistinguishable to each other and the color change became uniform over the exposed area, confirming sufficient conduction paths were made between WO_3 and underlying Si by dielectric breakdown of SiO_x .

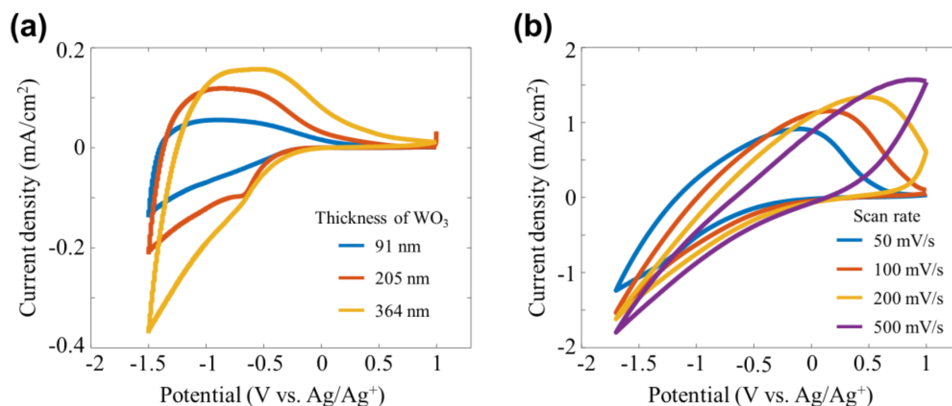

Figure 19. Cyclic voltammograms of WO_3 film deposited on highly doped Si substrate in 100 mM $LiClO_4$ electrolyte (acetonitrile) varying (a) thickness and (b) scan rate.

The WO_3 film shows the reversible charging and discharging of Li^+ as shown in the cyclic voltammetry (CV) conducted at 5 mV/s (Figure 19a). The current density and the thickness of the film show positive relationship, because the Li^+ charging capacity is proportional to the thickness of the film. At the film thickness of 364 nm, Li charging/discharging characteristics deviates more from ideal capacitor behavior. It would be resulted from the increasing resistance of the film. CVs obtained at higher scan rates (100 to 500 mV/s) are presented in Figure 19b, which show ohmic behavior with a scan rate dependence of current, b=0.099 in

i=a(dV/dt)^b. Moreover, additional overpotential is required for the de-intercalation of Li^+ at higher scan rate. This quasi-capacitive character would be resulted from the slow diffusivity of Li^+ in WO_3. Phase change of Li^+ conducting oxides was observed via CVs in previous literatures, however, no obvious feature was observed, showing that the amorphous nature of WO_3. The reduced overpotential is observed after the 2nd cycle at higher scan rates, which infers the residual Li that could not escape from the film facilitates the Li intercalation kinetics.

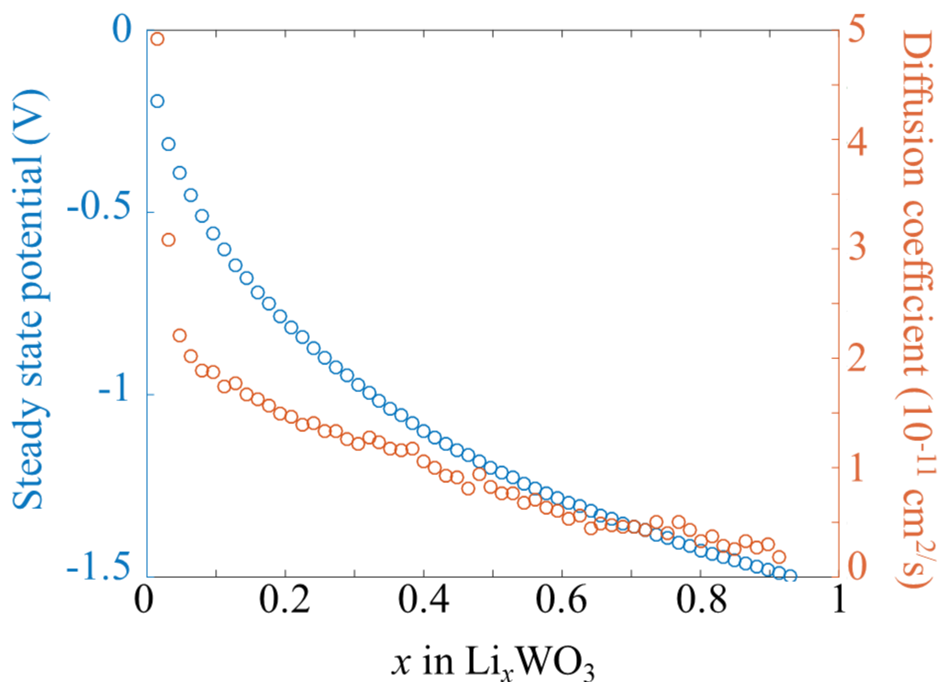

Figure 20. Steady state potential and diffusion coefficient of Li in Li_xWO_3 obtained via galvanostatic intermittent titration technique (GITT).

The steady state potential versus the stoichiometry, x, of Li_xWO_3 and the diffusivity of Li^+ at various Li^+ content were obtained by galvanostatic intermittent titration technique (GITT) conducted at various compositions (Figure 20). GITT is a useful technique to find out the diffusivity of foreign species that can intercalate into the thin layer. In GITT experiment, current ramp is applied for short time period to intercalate the species, Li^+ in this work. By relaxing the system at open circuit condition for a sufficiently long time, the steady state potential for certain stoichiometry can be obtained. The steady state potential shows linear relationship

to x, utilizing the voltage ramp to modulate the amount of Li^+ in device operation. The detailed method for extracting diffusion coefficient by GITT was established by Weppner et al..[92] Briefly, the diffusion coefficient is extracted from the slope of coulometric titration curve at open circuit relaxing condition (steady state potential versus Li content) and chronopotentiometric curve at current ramp period (cell potential versus square route of time). Then the equation for chemical diffusion constant (D) is derived to be

$$D = \frac{4}{\pi}\left(\frac{m_B V_M}{M_B S}\right)^2 \left[\frac{\Delta E_s}{\tau\left(dE/d\sqrt{t}\right)}\right]^2 \quad \text{(7)}$$

where m_B, M_B and V_M is the mass, the atomic mass and molar volume of WO_3, S is the area of the WO_3 film, E_s is the slope of coulometric titration curve, τ is the time of current ramp, and E is the cell potential during the current ramp period. D was calculated to be 4.91×10^{-11} cm^2s^{-1} at x=0.03 and D decreased with x. When the Li^+ content increases, there must be the electrostatic repulsion between Li cations, which results in slow diffusion in higher Li content as found in other literatures. According to the literature, the maximum intercalation capacity is 0.5 Li per formula unit for bulk (crystal structure) WO_3 and 1.12 for WO_3 nanorod.[14] However Li^+ capacity of our WO_3 film was ~0.9, and the voltammetric response was reversible despite the high electrochemical stress induced to the film.

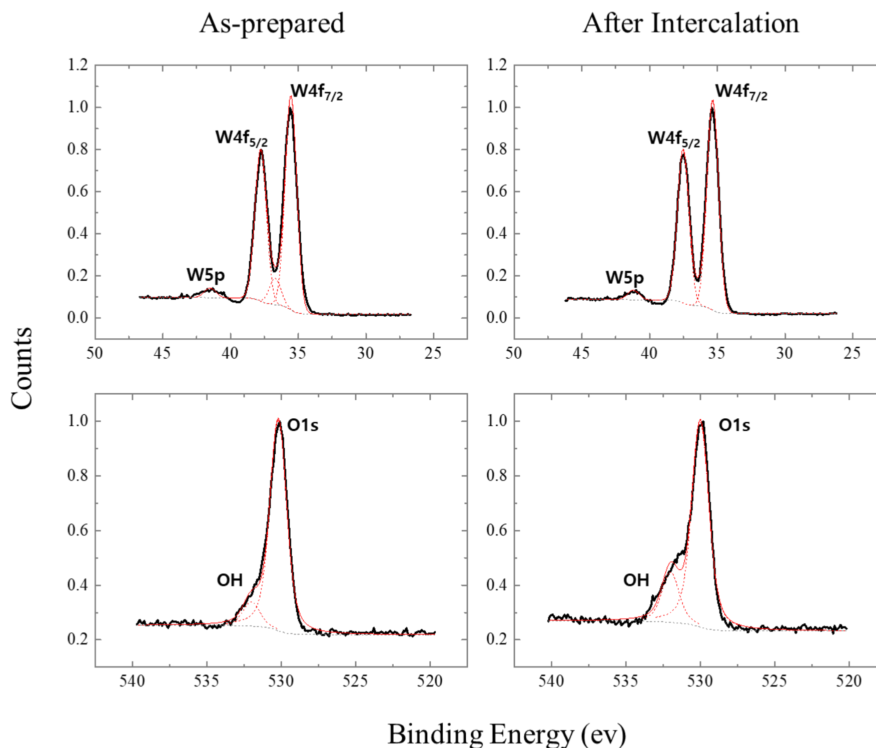

Figure 21. X-ray photoelectron spectra of (left) as-prepared WO_3 film in the region of W (upper-left) and O (bottom-left). X-ray photoelectron spectra of WO_3 after Li intercalation are presented on the right column in the region of W (upper-right) and O (bottom-right).

Because no further annealing after deposition was made, the amorphous film was expected to be obtained. The structure of WO_3 film is characterized by X-ray photoelectron spectroscopy (XPS) (Figure 21) and X-ray diffraction (XRD) (Figure 22). XPS spectra clearly confirms the identity of film to be tungsten trioxide, which has a little oxygen deficiency ($WO_{2.7}$).[93] The deficiency would be originated from the insufficient amount of oxygen gas in the sputter chamber, however, oxygen

partial pressure is set to be below 1.5 mTorr for preventing a possible oxidation damage of substrates. A shoulder arises on the O_{1s} band obtained at the surface of WO_3 after the Li intercalation in acetonitrile, which infers that the surface oxygen is reduced to hydroxyl group. The surface hydroxyl group would be resulted from the inevitable water content in organic solvents, however the wetting was not observed at the bulk region. XRD pattern of WO_3 film shows broad peaks of (200), (022), (202) which show its amorphous nature.[94]

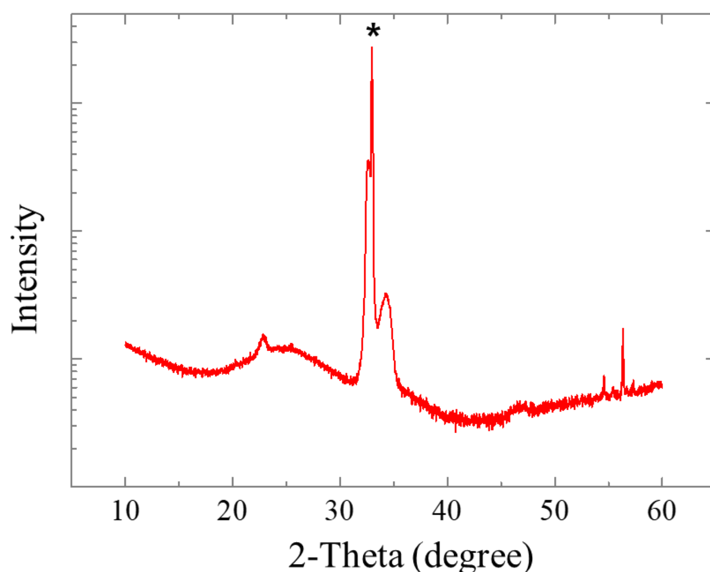

Figure 22. X-ray diffraction spectrum of WO_3 thin film deposited on highly doped Si wafer.

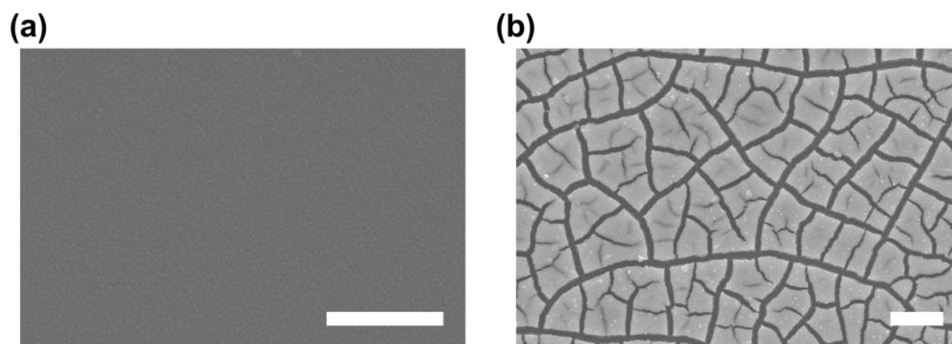

Figure 23. Scanning electron microscopy image of (a) as-sputtered WO_3 film and (b) WO_3 after Li intercalation/de-intercalation cycle.

Morphology analysis was conducted with scanning electron microscopy (SEM). As shown in Figure 23, as prepared amorphous WO_3 film has flat and smooth surface. Cracks were generated after repetitive charging and discharging, however, the roughness of single domain divided by cracks did not change. This topological change would be resulted from the mechanical strain applied to WO_3 film. During the charging/discharging processes, the volumetric change of monoclinic WO_3 crystal structure is known to be 17%. Considering the amorphous WO_3 film comprised of the locally crystalline WO_3 clusters, the topological strain due to the ion intercalation would be less than that of crystalline WO_3. The generated cracks are the result of deformation, which is a stabilized structure that compensates for mechanical stress.

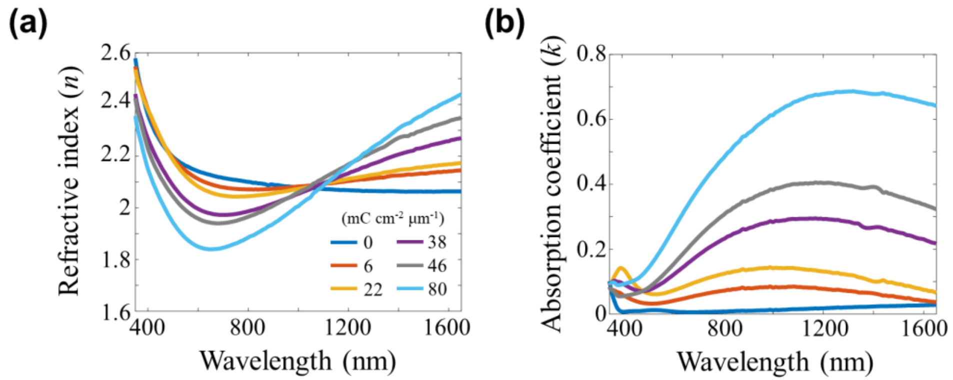

Figure 24. Optical properties of WO_3 thin film as a function of the amount of Li^+ injection. (a) Refractive index and (b) absorption coefficient measured with a range of wavelength between 350 nm to 1650 nm.

To obtain optical properties of WO_3 thin films incorporated in the proposed device, ellipsometry measurement was conducted using WO_3/Si. The WO_3 films with various charged states from bleached to charged state are characterized. The refractive index (n) and absorption coefficient (k) are measured at states corresponding to injected volumetric charge densities of 0, 6, 22, 38, 46, and 80 mC cm^{-2} μm^{-1} which correspond to the Li content, x, of 0.025, 0.088, 0.15, 0.18 and 0.32, respectively (Figure 24). Each state is called state 1 to 6 for convenience. One can see the apparent change of n and k, and this change is sufficient to be exploited as color display. In the visible regime, the measured results show a tendency of decreasing n and increasing k at the higher charge-injected state. In particular, the change of k by ion injection becomes much larger at the longer wavelength. This property is directly related to the fact that the dark state of WO_3

achieved by sufficient charge injection is deep blue.

Although there is topological change after Li^+ intercalation/de-intercalation cycles, the voltammetric response and optical properties are reversible during the repetitive Li^+ transportation. This reversibility, which would be ascribed to the structural stabilization by micrometer-scale domains created after the Li^+ intercalation/de-intercalation cycles, is a critical advantage for practical device operation. Therefore, we could conclude that the amorphous WO_3 film is suitable for electrochemically tunable optical device which employs sophisticated structure for better optical performance.

3.3.2. Reflective type display using WO_3 thin film

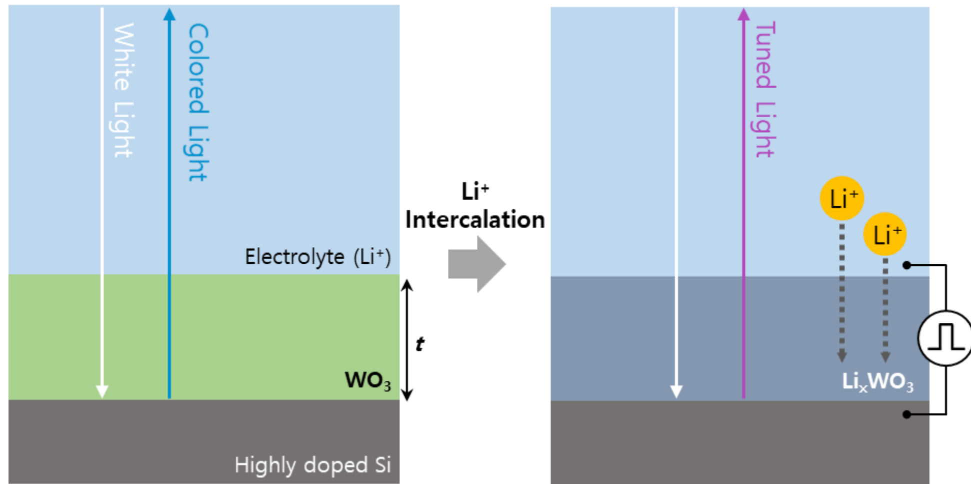

Figure 25. Schematic illustration of color generation and tuning mechanism of reflection-type device.

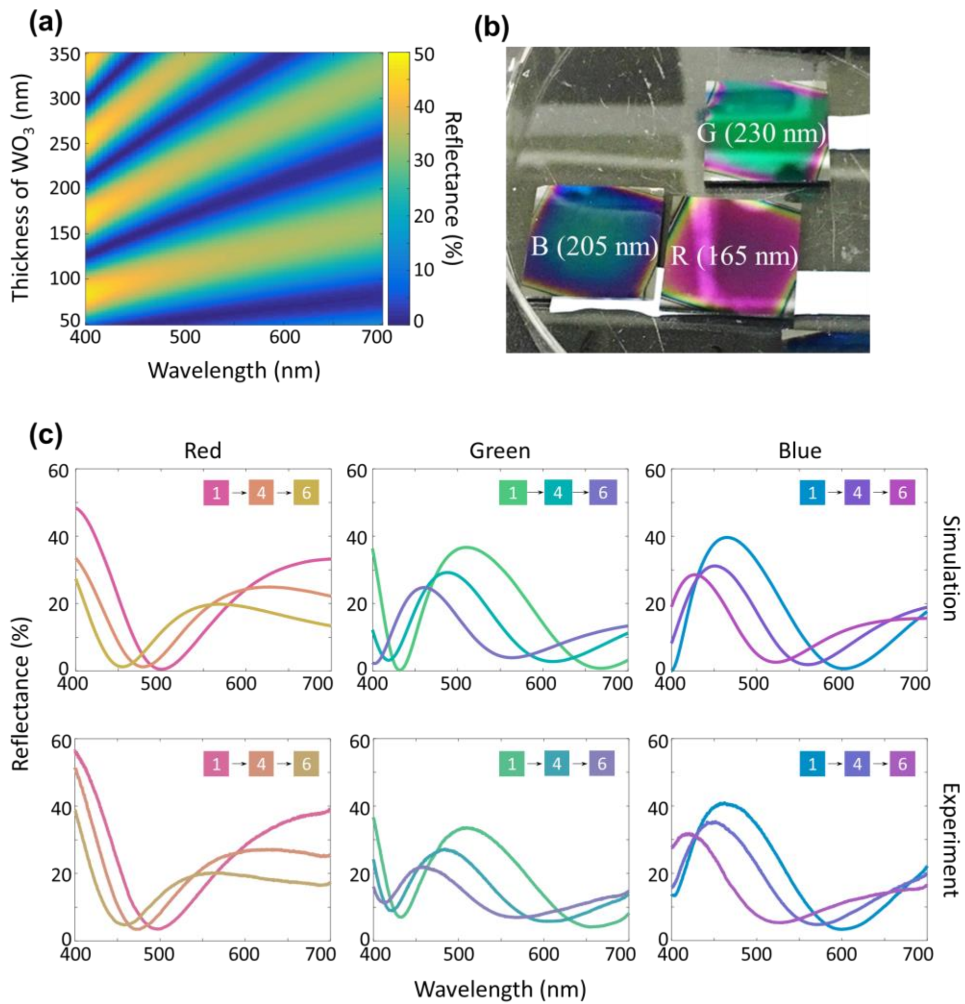

Figure 26. (a) Reflectance of WO_3 thin film on Si as a function of the incident wavelength and the thickness of WO_3. (b) Photographic image of fabricated red, green, and blue samples with target thickness. (c) Calculated (top) and experimental (bottom) spectra of reflected light. Color variation corresponding to each same colored spectrum from state 1 through 4 to 6 (inset).

The reflective type device employing WO_3 thin films is described in this section. As shown in the cross-sectional schematic of the reflective devices (Figure 25), the reflective device is basically WO_3/Si which was used to characterize electrical and optical behavior. A highly doped Si substrate serves as a reflector and an electrode, which lead to the abundant color expression due to the moderate reflectance of Si. The reflected light of the bleached-state WO_3/Si represents specific color, and the color can be tuned as WO_3 changes to Li_xWO_3 by Li^+ intercalation. The optical structure is designed to have resonance mode when the reflected light on the interface of electrolyte/WO_3 and WO_3/Si constructively and forms a cavity mode inside WO_3 film. This resonance leads to a decrease in reflectance due to the energy confinement in cavity. The thickness of WO_3 (t) determines the resonant wavelength so that a desired color generation can be achieved (Figure 26). In this configuration, the goal is to maximize reflectance in the desired wavelength region, while to suppress reflectance by placing the resonance in the unwanted region. In this respect, most noble metals are inappropriate to be utilized for the proposed as a reflector that have extremely low refractive indices and high absorption coefficient which result in high reflectivity compared to the reflectivity on the electrolyte/WO_3 boundary. The reflectivity can be simply calculated by Fresnel equation with normal incidence as

$$R = (|n_1 - n_2| - |n_1 + n_2|)^2 \qquad (8)$$

where n_1 and n_2 correspond to the refractive index of the different media,

respectively. When noble metals are used as a reflector, it is difficult to expect nearly zero reflectance under the resonance conditions. Thus the color of reflected light is blurred because the light of unwanted wavelength region cannot be completely eliminated when using noble metal reflectors. For this reason, a highly doped Si is selected as a reflector in the proposed device due to its moderate reflectivity and conductivity to be used as an electrode.

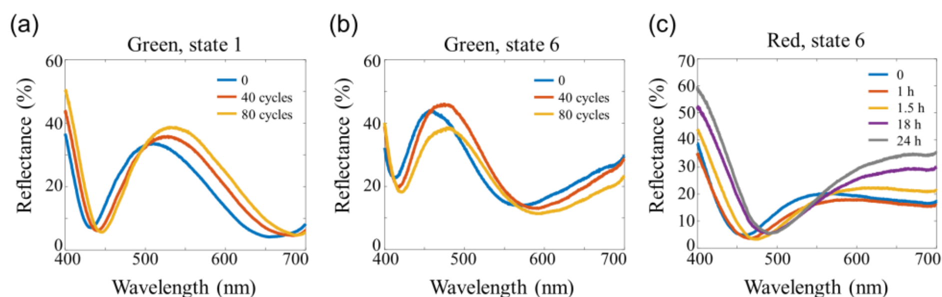

Figure 27. The reversibility and stability test of the reflective type devices. The spectrum change of a 235 nanometer-thick WO_3 on Si at state (a) 1 and (b) 6 for different Li^+ intercalation cycles. (c) The reflected spectra of a 165 nanometer-thick WO_3 on Si of state 6 after immersed in electrolyte.

Three primary colors, red, green, and blue, were expressed with the proposed devices and their color tuning by Li^+ injection are numerically calculated (top of Figure 26c). The thickness of WO_3 film are determined as 165 nm, 230 nm, and 205 nm for red, green, and blue, respectively. For all colors, the resonant dips show blue-shift for Li^+ intercalation due to decrease of refractive indices of WO_3. The experimental spectra of RGB devices and their colored states are presented in the

bottom of Figure 26c. The spectra show exceptionally good agreement between the simulation and experiment for all three colors. Also, its reversibility and stability were verified experimentally which showed sufficient reversibility over 80 cycles of Li^+ charging/discharging (Figure 27a, b). When the electrode was rested under open circuit condition after charging, it gradually discharged to its original state in 24 h (Figure 27c).

3.3.3. Transmissive type display using WO_3-based thin film

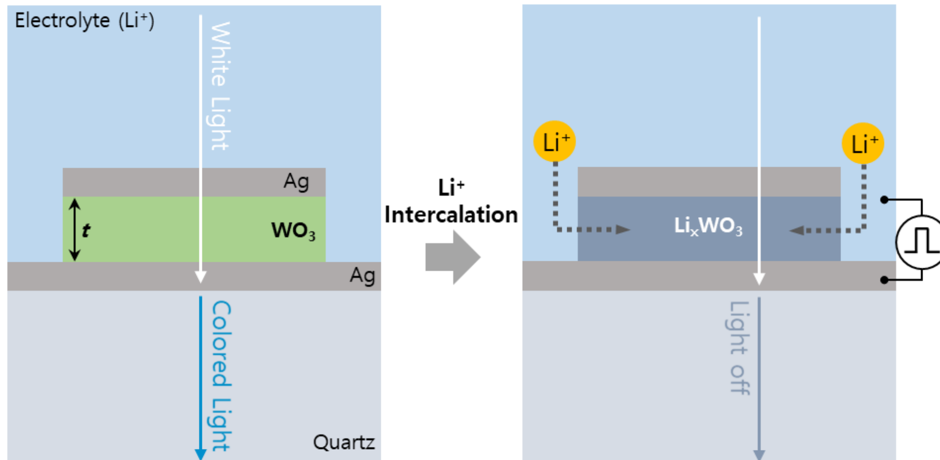

Figure 28. Schematic diagrams representing the working principle of transmissive type electrochromic device.

The reflective type display discussed in previous section has distinct advantages of simple structure and a large contact area with the electrolyte, which leads to fast response. However, it has a problem of poor color purity. In this section, the transmissive type color display based on WO_3 thin film is suggested which offers better color purity and on/off switching capability. The good color purity can be achieved without complex nanofabrication, therefore the centimeter-scale display applications would become possible using the transmissive type device purposed in this chapter.

Figure 28 shows the cross-sectional schematic of the transmissive type devices; the WO_3 is placed between two 40 nanometer-thick Ag layers. The

transmittance of this metal-insulator-metal configuration with normal incidence is well known as

$$T = \frac{1}{1+\frac{4R\sin^2 nk_0 t}{(1-R)^2}} \text{.........................(9)}$$

where R is power reflectance at the Ag / WO_3 interface, n is the real part of refractive index of WO_3, and t is the thickness of WO_3, respectively. When light is incident on the structure, reflected light on each Ag layer causes interference, and the Fabry-Pérot (FP) resonance occurs on the condition of constructive interference as $m\lambda=2nd$ in Equation 1, where m is the order of interference, λ is the wavelength of incidence. Under the normal incidence, the thickness of WO_3 (t) determines the resonant wavelength. In particular, the finesse (F) directly related to R is defined as

$$F = \frac{\pi\sqrt{R}}{1-R} \text{...........................(10)}$$

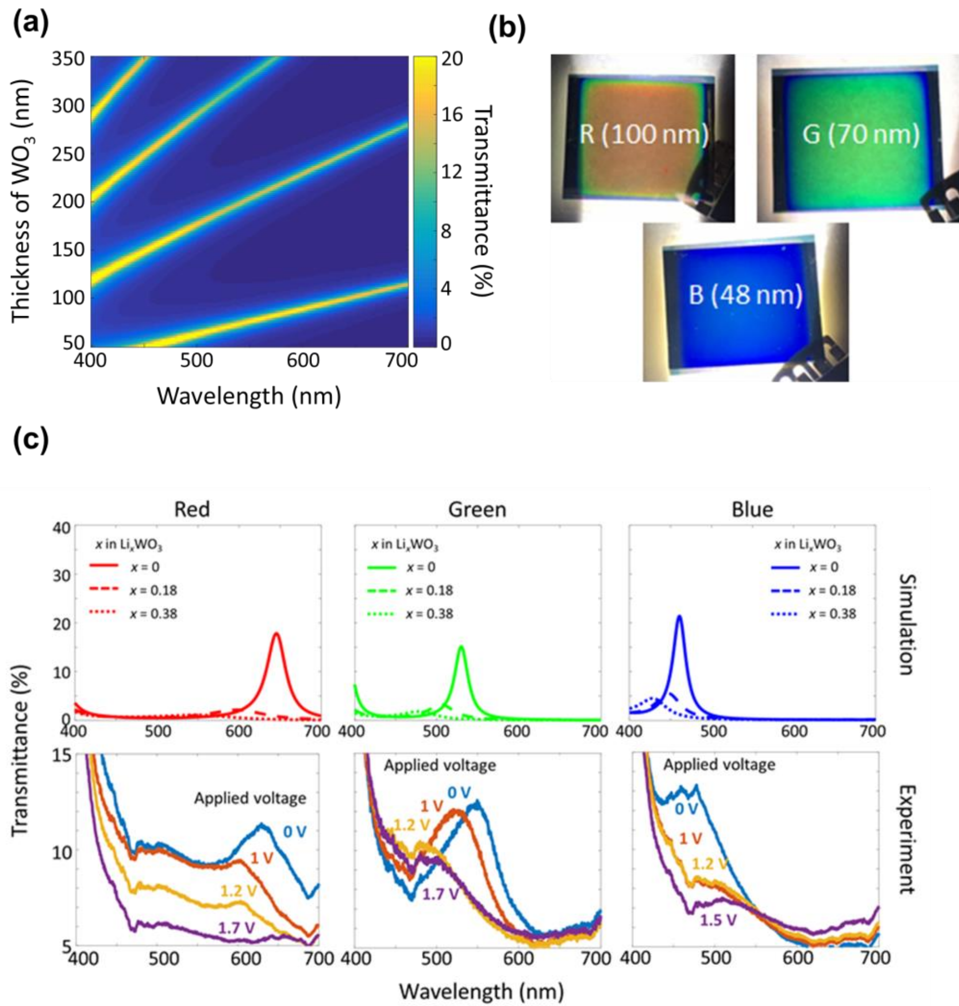

Figure 29. (a) Simulated transmittance of Ag/WO_3/Ag on quartz substrate as a function of the incident wavelength and the thickness of WO_3. (b) Photograph of primary devices (R, G and B) operates in transmissive type. (c) Simulated spectra tuning of transmitted light for R, G and B (top). Experimental spectra of transmissive devices showing switching capability.

It can be seen that the full width half maximum (FWHM) of the transmissive deivce can be much narrower and the purity of color can be enhanced as the reflectance at the WO_3/Ag interface increases. The transmission spectrum as a function of the thickness of WO_3 and the wavelength of incidence is numerically calculated (Figure 29a). For three primary color generation, the thickness of WO_3 is determined to be 100, 70 and 48 nm, for red, green and blue respectively (Figure 29 b).

The calculated and experimental spectrum of each transmissive device is presented in Figure 29c. The FWHM is broadened compared to the simulated spectrum. Unlike simulations that only consider vertical incidence to ideally flat interface, in experiments, the roughness of interfaces might scatter the light which results in the broadening of resonance. Thus the purity of color is poorer than expected.

The switching off of the transmissive device was successfully conducted by applying more negative potential than reflective device, to overcome the sluggish mass transfer of the horizontal direction in the WO_3 layer. Because of its structure, the only entrance of Li transport is its side, thus the expected response time is hundreds of seconds. By applying the DC voltage with -1 V to -1.7 V, the transmissvie device switched off stepwisely as predicted. As shown in the optical microscope image of transmissive device, the colored state did not show the color gradient, but the spotted pigmentation was observed. This implies the pinholes in the top Ag layer would facilitate the Li diffusion by providing vertical pathway.

3.4. Summary

The nanometer-thick WO_3 was successfully incorporated to the electrochromic nano-optical device, showing wide and rich color expression and switching capability. The devices that solely depend on the light absorption of WO_3 film should employ thicker film to lengthen the light path. Thus they have the disadvantages of large power consumption and slow response time. On the other hand, in this thesis, the weak light modulation capability due to reduced thickness of WO_3 is overcome by the designed nanostructure with sophisticated material selection. Si is generally considered as a poor reflector, however, the WO_3/Si system was able to represent rich color due to its moderate reflectance. The resonance wavelength blue shifted as Li^+ was intercalated into the WO_3 with reduced reflectance and turned back to the uncharged state reversibly. The transmissvie device constructed with WO_3 thin film showed better color purity compared to the reflective type device due to its metal-insulator-metal structure which can trap light more efficiently. The Li intercalation turned off the device with a diminished-blue-shifted resonance in the intermediated states. The fast reversibility has not been achieved due to the dissolution of top Ag layer, however, could be implemented by employing thin dielectric layer at WO_3/Ag_{top} interface or by substituting the top Ag to electrochemically stable metals. The full-colored smart window and electronic paper is expected to be developed by further optimization of these conceptual devices.

4. Conclusion

In this thesis, the electrochemical systems based on EOS were discussed. In chapter 2, the factors affecting the electrochemical behavior of EOS system employing dielectric material in the middle was analyzed. It was found that the chemical nature of the electrolyte induces significant difference in the conduction compared to MOS system. The experimental result was affected significantly by the cations in the electrolyte, because the cations in electrolyte modify the local electric field by adsorption and intercalation. The role of protons was able to be understood in the same manner. The surface potential built by the protonation of electrolyte/oxide interface was found to change the net electric field applied to the oxide. Thus the conduction and the accompanying dielectric breakdown under cathodic bias were accelerated at lower pH. When the ionic species that can transport from electrolyte to dielectric were present, the surface potential acted as a barrier of mass transport which can result in the inverted tendency of conduction versus pH. The electrical resistance of electrolyte/oxide interface was affected by the chemical composition of electrolyte. The surface adsorptive redox species could affect the resistance, however, only the role of redox species that can be reduced via outer sphere electron transfer was discussed. The well-known redox molecule, ruthenium hexamine (III), enhanced the electron transfer rate of EOS system. Dielectric breakdown, contrary to common knowledge, was not affected by the current increase.

Further experimental analysis is required regarding on the systems which represent the real system better such as electrolyte/metal(catalyst)/oxide /semiconductor. In such complex systems, oxides work as a protective layer which not only prevent the unwanted behavior or damage due to the electrochemical reaction on the underlying electrode, but also allow smooth electron flow between electrode and catalysts. Therefore, employing thinner oxide would be advantageous, which leads to stronger electric field and more charge conduction applied to the oxide. Understanding conduction and breakdown mechanism that can represent the electrode for electrocatalyst will contribute to developing stable and efficient electrocatalyst.

In chapter 3, the strategy was proposed to improve the optical performance of electrochromic device which operates in EOS system. Nanostructure which surrounded the key switchable material, WO_3, enabled the wide color expression although the amount of WO_3 was much smaller than the conventional WO_3-based electrochromic devices. The devices proposed in this dissertation could not achieve the sufficient response time and reversibility during operation. However, the good color purity attained without cutting-edge fabrication technique such as e-beam lithography or focused ion beam milling opens the possibility for commercialization after further optimization in structure and material selection.

Reference

(1) Lorenz, M.; Ramachandra Rao, M. S.; Venkatesan, T.; Fortunato, E.; Barquinha, P.; Branquinho, R.; Salgueiro, D.; Martins, R.; Carlos, E.; Liu, A.; et al. The 2016 Oxide Electronic Materials and Oxide Interfaces Roadmap. *J. Phys. D. Appl. Phys.* **2016**, *49*.

(2) Huang, Y. W.; Lee, H. W. H.; Sokhoyan, R.; Pala, R. A.; Thyagarajan, K.; Han, S.; Tsai, D. P.; Atwater, H. A. Gate-Tunable Conducting Oxide Metasurfaces. *Nano Lett.* **2016**, *16*, 5319–5325.

(3) Buch, V. R.; Chawla, A. K.; Rawal, S. K. Review on Electrochromic Property for WO3 Thin Films Using Different Deposition Techniques. *Mater. Today Proc.* **2016**, *3*, 1429–1437.

(4) Ahn, H. S.; Bard, A. J. Single-Nanoparticle Collision Events: Tunneling Electron Transfer on a Titanium Dioxide Passivated n-Silicon Electrode. *Angew. Chemie - Int. Ed.* **2015**, *54*, 13753–13757.

(5) Lin, Y.; Kapadia, R.; Yang, J.; Zheng, M.; Chen, K.; Hettick, M.; Yin, X.; Battaglia, C.; Sharp, I. D.; Ager, J. W.; et al. Role of TiO2 Surface Passivation on Improving the Performance of P-InP Photocathodes. *J. Phys. Chem. C* **2015**, *119*, 2308–2313.

(6) Li, J. F.; Tian, X. D.; Li, S. B.; Anema, J. R.; Yang, Z. L.; Ding, Y.; Wu, Y. F.; Zeng, Y. M.; Chen, Q. Z.; Ren, B.; et al. Surface Analysis Using Shell-Isolated Nanoparticle-Enhanced Raman Spectroscopy. *Nat. Protoc.* **2013**, *8*, 52–65.

(7) Chen, Y. W.; Prange, J. D.; Dühnen, S.; Park, Y.; Gunji, M.; Chidsey, C. E. D.; McIntyre, P. C. Atomic Layer-Deposited Tunnel Oxide Stabilizes Silicon Photoanodes for Water Oxidation. *Nat. Mater.* **2011**, *10*, 539–544.

(8) Hu, S.; Shaner, M. R.; Beardslee, J. A.; Lichterman, M.; Brunschwig, B. S.; Lewis, N. S. Amorphous TiO2 Coatings Stabilize Si, GaAs, and GaP Photoanodes for Efficient Water Oxidation. *Science (80-.).* **2014**, *344*, 1005–1009.

(9) Daniele, I. Resistive Switching Memories Based on Metal Oxides: Mechanisms, Reliability and Scaling. *Semicond. Sci. Technol.* **2016**, *31*, 63002.

(10) Fowler, B. W.; Chang, Y.-F.; Zhou, F.; Wang, Y.; Chen, P.-Y.; Xue, F.; Chen, Y.-T.; Bringhurst, B.; Pozder, S.; Lee, J. C. Electroforming and Resistive Switching in Silicon Dioxide Resistive Memory Devices. *RSC Adv.* **2015**, *5*, 21215–21236.

(11) Jung, S. C.; Han, Y. K. How Do Li Atoms Pass through the Al2O3 Coating Layer during Lithiation in Li-Ion Batteries? *J. Phys. Chem. Lett.* **2013**, *4*, 2681–2685.

(12) Jung, S. C.; Kim, H. J.; Choi, J. W.; Han, Y. K. Sodium Ion Diffusion in Al2O3: A Distinct Perspective Compared with Lithium Ion Diffusion. *Nano Lett.* **2014**, *14*, 6559–6563.

(13) Liu, Z.; Yu, Q.; Zhao, Y.; He, R.; Xu, M.; Feng, S.; Li, S.; Zhou, L.; Mai, L. Silicon Oxides: A Promising Family of Anode Materials for Lithium-Ion Batteries. *Chem. Soc. Rev.* **2019**, *48*, 285–309.

(14) He, Y.; Gu, M.; Xiao, H.; Luo, L.; Shao, Y.; Gao, F.; Du, Y.; Mao, S. X.; Wang, C. Atomistic Conversion Reaction Mechanism of WO3 in Secondary Ion Batteries of Li, Na, and Ca. *Angew. Chemie - Int. Ed.* **2016**, *55*, 6244–6247.

(15) Leighton, C. Electrolyte-Based Ionic Control of Functional Oxides. *Nat. Mater.* **2019**, *18*, 13–18.

(16) Fowler, B. W.; Chang, Y.-F.; Zhou, F.; Wang, Y.; Chen, P.-Y.; Xue, F.; Chen, Y.-T.; Bringhurst, B.; Pozder, S.; Lee, J. C. Electroforming and Resistive Switching in Silicon Dioxide Resistive Memory Devices. *RSC Adv.* **2015**, *5*, 21215–21236.

(17) Von Der Heiden, A.; Bornhöfft, M.; Mayer, J.; Martin, M. Oxygen Diffusion in Amorphous and Partially Crystalline Gallium Oxide. *Phys. Chem. Chem. Phys.* **2019**, *21*, 4268–4275.

(18) El-Sayed, A. M.; Watkins, M. B.; Grasser, T.; Afanas'Ev, V. V.; Shluger, A. L. Hydrogen-Induced Rupture of Strained SiO Bonds in Amorphous Silicon Dioxide. *Phys. Rev. Lett.* **2015**, *114*, 1–5.

(19) Godet, J.; Pasquarello, A. Proton Diffusion Mechanism in Amorphous SiO2. *Phys. Rev. Lett.* **2006**, *97*, 1–4.

(20) Sheikholeslam, S. A.; Manzano, H.; Grecu, C.; Ivanov, A. Reduced Hydrogen Diffusion in Strained Amorphous SiO2: Understanding Ageing in MOSFET Devices. *J. Mater. Chem. C* **2016**, *4*, 8104–8110.

(21) Vanheusden, K.; Devine, R. a. B. The Role of Interface States in Hydrogen-Annealing-Induced Mobile Proton Generation at the Si–SiO[Sub 2] Interface. *Appl. Phys. Lett.* **2000**, *76*, 3109.

(22) Godet, J.; Pasquarello, A. Protons at the Si-SiO2 Interface: A First Principle Investigation. *Microelectron. Eng.* **2007**, *84*, 2035–2038.

(23) Osburn, C. M.; Raider, S. I. The Effect of Mobile Sodium Ions on Field Enhancement Dielectric Breakdown in SiO[Sub 2] Films on Silicon. *J. Electrochem. Soc.* **1973**, *120*, 1369.

(24) Osburn, C. M.; Ormond, D. W. Sodium-Induced Barrier-Height Lowering

and Dielectric Breakdown on SiO[Sub 2] Films on Silicon. *J. Electrochem. Soc.* **1974**, *121*, 1195.

(25) Derbenwick, G. F. Mobile Ions in SiO2: Potassium. *J. Appl. Phys.* **1977**, *48*, 1127–1130.

(26) Chiu, F. A Review on Conduction Mechanisms in Dielectric Films. *Adv. Mater. Sci. Eng.* **2014**, *2014*, 1–18.

(27) Abe, Y.; Hosono, H.; Lee, W. H.; Kasuga, T. Electrical Conduction Due to Protons and Alkali-Metal Ions in Oxide Glasses. *Phys. Rev. B* **1993**, *48*, 15621–15625.

(28) Fan, R.; Huh, S.; Yan, R.; Arnold, J.; Yang, P. Gated Proton Transport in Aligned Mesoporous Silica Films. *Nat. Mater.* **2008**, *7*, 303–307.

(29) Zhao, Y.; Liu, Z.; Sun, T.; Zhang, L.; Jie, W.; Wang, X.; Xie, Y.; Tsang, Y. H.; Long, H.; Chai, Y. Mass Transport Mechanism of Cu Species at the Metal/Dielectric Interfaces with a Graphene Barrier. *ACS Nano* **2014**, *8*, 12601–12611.

(30) Bousse, L.; Bergveld, P. The Role of Buried OH Sites in the Response Mechanism of Inorganic-Gate PH-Sensitive ISFETs. *Sensors and Actuators* **1984**, *6*, 65–78.

(31) Lee, J.-Y.; Lee, J. G.; Lee, S.-H.; Seo, M.; Piao, L.; Bae, J. H.; Lim, S. Y.; Park, Y. J.; Chung, T. D. Hydrogen-Atom-Mediated Electrochemistry. *Nat. Commun.* **2013**, *4*, 2766.

(32) Velmurugan, J.; Zhan, D.; Mirkin, M. V. Electrochemistry through Glass. *Nat. Chem.* **2010**, *2*, 498–502.

(33) Esposito, D. V.; Levin, I.; Moffat, T. P.; Talin, A. A. H2evolution at Si-Based Metal-Insulator-Semiconductor Photoelectrodes Enhanced by Inversion Channel Charge Collection and H Spillover. *Nat. Mater.* **2013**, *12*, 562–568.

(34) Vanheusden, K.; Warren, W. L.; Devine, R. A. B.; Fleetwood, D. M.; Schwank, J. R.; Shaneyfelt, M. R.; Winokur, P. S.; Lemnios, Z. J. Non-Volatile Memory Device Based on Mobile Protons in SiO2 Thin Films. *Nature*. 1997, pp 587–589.

(35) Briggs, K.; Charron, M.; Kwok, H.; Le, T.; Chahal, S.; Bustamante, J.; Waugh, M.; Tabard-Cossa, V. Kinetics of Nanopore Fabrication during Controlled Breakdown of Dielectric Membranes in Solution. *Nanotechnology* **2015**, *26*, 084004.

(36) Van Hal, R. E. G.; Eijkel, J. C. T.; Bergveld, P. A General Model to Describe the Electrostatic Potential at Electrolyte Oxide Interfaces. *Adv. Colloid Interface Sci.* **1996**, *69*, 31–62.

(37) Jaksic, J. M.; Labou, D.; Papakonstantinou, G. D.; Siokou, A.; Jaksic, M. M.

Novel Spillover Interrelating Reversible Electrocatalysts for Oxygen and Hydrogen Electrode Reactions. *J. Phys. Chem. C* **2010**, *114*, 18298–18312.

(38) Lombardo, S.; Stathis, J. H.; Linder, B. P.; Pey, K. L.; Palumbo, F.; Tung, C. H. Dielectric Breakdown Mechanisms in Gate Oxides. *J. Appl. Phys.* **2005**, *98*.

(39) Osburn, C. M.; Ormond, D. W. Dielectric Breakdown in Silicon Dioxide Films on Silicon. *J. Electrochem. Soc.* **2007**, *119*, 591.

(40) Cui, H.; Burke, P. A. Time-Dependent Dielectric Breakdown Studies of PECVD H:SiCN and H:SiC Thin Films for Copper Metallization. *J. Electrochem. Soc.* **2004**, *151*, G795.

(41) Wilshaw, R. S. B.; R, P. Potassium Ions in SiO2: Electrets for Silicon Surface Passivation. *J. Phys. D. Appl. Phys.* **2018**, *51*, 25101.

(42) Yun, J.; Cho, Y.-B.; Jang, W.; Lee, J. G.; Shin, S. J.; Han, S. H.; Lee, Y.; Chung, T. D. Dielectric Breakdown and Post-Breakdown Dissolution of Si/SiO<inf>2</Inf>Cathodes in Acidic Aqueous Electrochemical Environment. *Sci. Rep.* **2018**, *8*.

(43) Lee, J. G. J.-Y.; Lee, J. G. J.-Y.; Lee, S.-H.; Seo, M.; Piao, L.; Bae, J. H.; Lim, S. Y.; Park, Y. J.; Chung, T. D. Hydrogen-Atom-Mediated Electrochemistry. *Nat. Commun.* **2013**, *4*, 2766.

(44) Lee, J. G.; Lee, J.-Y.; Yun, J.; Lee, Y.; Lee, S.; Shin, S. J.; Bae, J. H.; Chung, T. D. Conduction through a SiO<inf>2</Inf>layer Studied by Electrochemical Impedance Analysis. *Electrochem. commun.* **2017**, *76*.

(45) Blöchl, P.; Stathis, J. Hydrogen Electrochemistry and Stress-Induced Leakage Current in Silica. *Phys. Rev. Lett.* **1999**, *83*, 372–375.

(46) Kwok, H.; Briggs, K.; Tabard-Cossa, V. Nanopore Fabrication by Controlled Dielectric Breakdown. *PLoS One* **2014**, *9*.

(47) Mibus, M.; Jensen, C.; Hu, X.; Knospe, C.; Reed, M. L.; Zangari, G. Dielectric Breakdown and Failure of Anodic Aluminum Oxide Films for Electrowetting Systems. *J. Appl. Phys.* **2013**, *114*.

(48) Liu, Y.; Hudak, N. S.; Huber, D. L.; Limmer, S. J.; Sullivan, J. P.; Huang, J. Y. In Situ Transmission Electron Microscopy Observation of Pulverization of Aluminum Nanowires and Evolution of the Thin Surface Al2O3 Layers during Lithiation-Delithiation Cycles. *Nano Lett.* **2011**, *11*, 4188–4194.

(49) Helms, C. R.; Poindexter, E. H. The Silicon-Silicon-Dioxide System : Its Microstructure and Imperfections. *Reports Prog. Phys.* **1994**, *57*, 791–852.

(50) Yeap, K. B.; Gall, M.; Liao, Z.; Sander, C.; Muehle, U.; Justison, P.; Aubel, O.; Hauschildt, M.; Beyer, A.; Vogel, N.; et al. In Situ Study on Low-k Interconnect Time-Dependent-Dielectric-Breakdown Mechanisms. *J. Appl. Phys.* **2014**, *115*.

(51) Ohring, M. *Reliability and Failure of Electronic Materials and Devices*; Academic Press, 1998.

(52) Dimaria, D. J.; Arnolda, D.; Watson, T. J.; Box, P. O.; Heights, Y.; York, N. Impact Ionization, Trap Creation, Degradation, Dioxide Films on Silicon and Breakdown in Silicon. *J. Appl. Phys.* **1993**, *73*, 3367–3384.

(53) Rashkeev, S. N.; Fleetwood, D. M.; Schrimpf, R. D.; Pantelides, S. T. Defect Generation by Hydrogen at the Si- SiO2 Interface. *Phys. Rev. Lett.* **2001**, *87*, 1–4.

(54) Yao, J.; Zhong, L.; Natelson, D.; Tour, J. M. In Situ Imaging of the Conducting Filament in a Silicon Oxide Resistive Switch. *Sci. Rep.* **2012**, *2*, 242.

(55) Revesz, a. G. The Role of Hydrogen in SiO2 Films on Silicon. *J. Electrochem. Soc.* **1979**, *126*, 122.

(56) Godet, J.; Pasquarello, A. Ab Initio Study of Charged States of H in Amorphous SiO2. *Microelectron. Eng.* **2005**, *80*, 288–291.

(57) Wimmer, Y.; Gös, W.; Grasser, T.; Shluger, A. L. Role of Hydrogen in Volatile Behaviour of Defects in SiO2 -Based Electronic Devices. *Proc. R. Soc. A Math. Phys. Eng. Sci.* **2016**, *472*, 20160009.

(58) Rashkeev, S. N.; Fleetwood, D. M.; Schrimpf, R. D.; Pantelides, S. T. Proton-Induced Defect Generation at the Si-SiO2 Interface. *IEEE Trans. Nucl. Sci.* **2001**, *48*, 2086–2092.

(59) Alves, J.; Baptista, J. The Behavior of Zeta Potential of Silica Suspensions. *New J. Glas. Ceram.* **2014**, *4*, 29–37.

(60) Beauvais, J.; Genest, J.; Baron, T.; Chamas, H.; Souifi, A.; Chevalier, C.; Cloarec, J.-P.; Chevolot, Y. PH Driven Addressing of Silicon Nanowires onto Si 3 N 4 /SiO 2 Micro-Patterned Surfaces . *Nanotechnology* **2016**, *27*, 295602.

(61) Pfeiffer-Laplaud, M.; Gaigeot, M. P. Electrolytes at the Hydroxylated (0001) α-Quartz/Water Interface: Location and Structural Effects on Interfacial Silanols by DFT-Based MD. *J. Phys. Chem. C* **2016**, *120*, 14034–14047.

(62) Tadros, T. F.; Lyklema, J. Adsorption of Potential-Determining Ions at the Silica-Aqueous Electrolyte Interface and the Role of Some Cations. *J. Electroanal. Chem. Interfacial Electrochem.* **1968**, *17*, 267–275.

(63) Zuyi, T.; Hongxia, Z. Acidity and Alkali Metal Adsorption on the SiO2-Aqueous Solution Interface. *J. Colloid Interface Sci.* **2002**, *252*, 15–20.

(64) Shacham-Diamand, Y. Copper Transport in Thermal SiO[Sub 2]. *J. Electrochem. Soc.* **1993**, *140*, 2427.

(65) Abel, B.; Buck, U.; Sobolewski, A. L.; Domcke, W. On the Nature and

Signatures of the Solvated Electron in Water. *Phys. Chem. Chem. Phys.* **2012**, *14*, 22–34.

(66) Buxton, G. V.; Greenstock, C. L.; Helman, W. P.; Ross, A. B. Critical Review of Rate Constants for Reactions of Hydrated Electrons, Hydrogen Atoms and Hydroxyl Radicals (???OH/???O??? In Aqueous Solution. *J. Phys. Chem. Ref. Data* **1988**, *17*, 513–886.

(67) Carlsen, A. T.; Briggs, K.; Hall, A. R.; Tabard-Cossa, V. Solid-State Nanopore Localization by Controlled Breakdown of Selectively Thinned Membranes. *Nanotechnology* **2017**, *28*, 085304.

(68) Kresse, G.; Furthmüller, J. Efficient Iterative Schemes for Ab Initio Total-Energy Calculations Using a Plane-Wave Basis Set. *Phys. Rev. B - Condens. Matter Mater. Phys.* **1996**, *54*, 11169–11186.

(69) Perdew, J. P.; Burke, K.; Ernzerhof, M. The Stability of Ionic Crystal Surfaces. Journal of Physics C: Solid State Physics, 12(22), 4977. **1996**, *77*, 3865–3868.

(70) Chadi, D. J. Special Points for Brillouin-Zone Integrations. *Phys. Rev. B* **1977**, *16*, 1746–1747.

(71) Ong, S. P.; Richards, W. D.; Jain, A.; Hautier, G.; Kocher, M.; Cholia, S.; Gunter, D.; Chevrier, V. L.; Persson, K. A.; Ceder, G. Python Materials Genomics (Pymatgen): A Robust, Open-Source Python Library for Materials Analysis. *Comput. Mater. Sci.* **2013**, *68*, 314–319.

(72) L., V. Computer “Exyeriments” on Classical Fluids. I. Thermodynamical Properties of Lennard-Jones Molecules. *Phys. Rev.* **1967**, *159*, 183–195.

(73) Nosé, S. A Unified Formulation of the Constant Temperature Molecular Dynamics Methods. *J. Chem. Phys.* **1984**, *81*, 511–519.

(74) Hoover, W. G. Hoover WG (1985) Canonical Dynamics: Equilibrium Phase-Space Distributions. Phys Rev A 31:1695–1697 . Doi: 10.1103/PhysRevA.31.1695. **1985**, *31*, 1695–1697.

(75) Fromherz, P. Threshold Voltage of the EOSFET: Reference Electrode and Oxide-Electrolyte Interface. *Phys. status solidi* **2012**, *209*, 1157–1162.

(76) Yoshihiro Abe; Hideo Hosono; Yoshio Ohta; L. L. Hench. Protonic Conduction in Oxide Glasses: Simple Relations between Electrical Conductivity, Activation Energy, and the o-h Bonding State. *Phys. Rev. B* **1988**, *38*, 10166–10169.

(77) Kotama, M. Evidence for Protonic Conduction in Alkali-Free Phosphate Glasses. *J. Electrochem. Soc.* **2006**, *138*, 2928.

(78) Marcus, Y. Ion Solvation. WILEY, **1985**.

(79) Watanabe, H.; Baba, T.; Ichikawa, M. Characterization of Local Dielectric

Breakdown in Ultrathin SiO2 Films Using Scanning Tunneling Microscopy and Spectroscopy. *J. Appl. Phys.* **1999**, *85*, 6704–6710.

(80) Wilson, H. F.; Barnard, A. S. Predictive Morphology Control of Hydrogen-Terminated Silicon Nanoparticles. *J. Phys. Chem. C* **2014**, *118*, 2580–2586.

(81) Jiang, H.; Hong, J. J.; Wu, X.; Surta, T. W.; Qi, Y.; Dong, S.; Li, Z.; Leonard, D. P.; Holoubek, J. J.; Wong, J. C.; et al. Insights on the Proton Insertion Mechanism in the Electrode of Hexagonal Tungsten Oxide Hydrate. *J. Am. Chem. Soc.* **2018**, *140*, 11556–11559.

(82) Wang, H.; Wang, X.; Yan, C.; Zhao, H.; Zhang, J.; Santschi, C.; Martin, O. J. F. Full Color Generation Using Silver Tandem Nanodisks. *ACS Nano* **2017**, *11*, 4419–4427.

(83) Duempelmann, L.; Luu-Dinh, A.; Gallinet, B.; Novotny, L. Four-Fold Color Filter Based on Plasmonic Phase Retarder. *ACS Photonics* **2016**, *3*, 190–196.

(84) Park, C. S.; Shrestha, V. R.; Yue, W.; Gao, S.; Lee, S. S.; Kim, E. S.; Choi, D. Y. Structural Color Filters Enabled by a Dielectric Metasurface Incorporating Hydrogenated Amorphous Silicon Nanodisks. *Sci. Rep.* **2017**, *7*, 1–9.

(85) Yue, W.; Gao, S.; Lee, S. S.; Kim, E. S.; Choi, D. Y. Subtractive Color Filters Based on a Silicon-Aluminum Hybrid-Nanodisk Metasurface Enabling Enhanced Color Purity. *Sci. Rep.* **2016**, *6*, 1–7.

(86) Ye, T.; Xiang, Y.; Ji, H.; Hu, C.; Wu, G. Electrodeposition-Based Electrochromic Devices with Reversible Three-State Optical Transformation by Using Titanium Dioxide Nanoparticle Modified FTO Electrode. *RSC Adv.* **2016**, *6*, 30769–30775.

(87) Araki, S.; Nakamura, K.; Kobayashi, K.; Tsuboi, A.; Kobayashi, N. Electrochemical Optical-Modulation Device with Reversible Transformation between Transparent, Mirror, and Black. *Adv. Mater.* **2012**, *24*, 122–126.

(88) Xiong, K.; Emilsson, G.; Maziz, A.; Yang, X.; Shao, L.; Jager, E. W. H.; Dahlin, A. B. Electronic Paper: Plasmonic Metasurfaces with Conjugated Polymers for Flexible Electronic Paper in Color (Adv. Mater. 45/2016). *Adv. Mater.* **2016**, *28*, 10103–10103.

(89) Xiong, K.; Tordera, D.; Emilsson, G.; Olsson, O.; Linderhed, U.; Jonsson, M. P.; Dahlin, A. B. Switchable Plasmonic Metasurfaces with High Chromaticity Containing Only Abundant Metals. *Nano Lett.* **2017**, *17*, 7033–7039.

(90) Sterl, F.; Strohfeldt, N.; Walter, R.; Griessen, R.; Tittl, A.; Giessen, H. Magnesium as Novel Material for Active Plasmonics in the Visible Wavelength Range. *Nano Lett.* **2015**, *15*, 7949–7955.

(91) Holsteen, A. L.; Raza, S.; Fan, P.; Kik, P. G.; Brongersma, M. L. Purcell Effect for Active Tuning of Light Scattering from Semiconductor Optical Antennas. *Science (80-.).* **2017**, *358*, 1407–1410.

(92) Weppner, W. Determination of the Kinetic Parameters of Mixed-Conducting Electrodes and Application to the System Li[Sub 3]Sb. *J. Electrochem. Soc.* **1977**, *124*, 1569.

(93) Ji, R.; Zheng, D.; Zhou, C.; Cheng, J.; Yu, J.; Li, L. Low-Temperature Preparation of Tungsten Oxide Anode Buffer Layer via Ultrasonic Spray Pyrolysis Method for Large-Area Organic Solar Cells. *Materials (Basel).* **2017**, *10*, 820.

(94) Liu, F.; Chen, X.; Xia, Q.; Tian, L.; Chen, X. Ultrathin Tungsten Oxide Nanowires: Oleylamine Assisted Nonhydrolytic Growth, Oxygen Vacancies and Good Photocatalytic Properties. *RSC Adv.* **2015**, *5*, 77423–77428.

국문 초록

산화물의 전기적 특성에 대한 이해는 전자소재 분야에서 중요한 이슈로 다루어졌다. 최근 들어 산화물이 전해질과 접한 상태에서 작동하도록 요구하는 시스템이 중요하게 연구되고 있다. 배터리, 전기촉매로 구성된 에너지 변환 장치, 전기화학적으로 제어되는 장효과 트랜지스터 (field effect transistor, FET) 등이 그것이다. 이와 같은 장치들의 성능 및 안정성을 개선하기 위해서는 전해질과 계면을 이루는 산화물의 전기적 특성을 깊이 있게 이해하는 것이 선행되어야 한다. 이에 본 학위논문에서는 전해질/산화막/도체로 구성된 시스템의 전도현상에 대해 다루었다. 전해질에 속한 화학종들이 시스템의 전도도 및 절연파괴에 미치는 영향에 대해 분석하였으며, 전해질/산화막 계면에서 일어나는 현상을 중심으로 이를 이해하였다. 양성자를 포함한 이온종 및 전기화학적 반응종의 역할과 그들간의 상호작용이 계면 및 산화막 내부의 전도 기작에 큰 영향을 끼침을 실험적으로 밝혔으며 이론적으로 현상을 설명하였다. 이러한 기초적인 시스템에 대한 이해뿐만 아니라 높은 이온 전도도를 갖는 산화박막이 활용된 새로운 개념의 전기변색소자에 대해서 학위논문을 통해 제안하였다. 큰 밴드갭을 가진 산화물이 외부의 이온을 머금게 되면 전기적 성질이 변함과 동시에 광학적 성질 역시 변한다. 이를 전기변색 현상이라 하는데, 전자종이, 지능형 창호 개발을 목적으로 연구되고 있

다. 다양한 개념의 전기변색 소자가 제안되었으나 대부분이 단순히 명암 제어에 그치고 있으며 특정 색상을 표현하는 경우에도 색의 순도가 낮은 한계를 가지고 있다. 텅스텐 산화물(WO_3)은 대표적인 전기변색물질로써 앞서 언급된 한계를 갖고 있다. 이에 본 연구에서는 WO_3 주위에 효율적으로 설계된 나노구조체를 도입함으로써 이와 같은 한계를 극복할 수 있음을 보이고자 한다. 가시광선 대역에서 폭넓은 색 표현이 가능한 투과 및 반사형의 광소자가 구현되었으며 공진 파장 및 빛의 세기를 전기변색의 원리에 입각하여 제어할 수 있음을 보였다.

핵심어: 전해질/산화물/전극 시스템, 절연파괴, 절연피막, 전기변색, 텅스텐 산화박막, 나노광학